

₁ Low p_T dielectron production in Au+Au collisions at
₂ $\sqrt{s_{NN}} = 200$ GeV and U+U collisions at $\sqrt{s_{NN}} = 193$
₃ GeV at STAR

₄ Shuai Yang
₅ syang@rcf.rhic.bnl.gov

May 17, 2018

6 Contents

7	1	Data Set and Event Selection	3
8	2	Electron Identification	5
9	2.1	Track Selection	5
10	2.2	Electron Identification Cuts	5
11	2.3	Electron Purity	7
12	3	Pair Reconstruction and Background Subtraction	9
13	3.1	Like-sign Technique	14
14	3.2	Mixed-Event Technique	15
15	3.3	Photon Conversion Removal	17
16	3.4	Raw Signals	21
17	4	Efficiency and Acceptance Corrections	22
18	4.1	Single Track Efficiency	22
19	4.1.1	TPC Tracking Efficiency	30
20	4.1.2	nHitsDedx Cut Efficiency	30
21	4.1.3	TOF Matching Efficiency	31
22	4.1.4	eID Cuts Efficiency	32
23	4.2	Pair Efficiency	33
24	5	Hadronic Cocktail Simulation	38
25	6	Systematic Uncertainties	46
26	7	Physics Results	51
27	7.1	Consistency Check Between Run10 and Run11 Au + Au Collisions	51
28	7.2	Low p_T e^+e^- Paper Plots	51

29 1 Data Set and Event Selection

30 The data sets used in this analysis are from Au + Au collisions at $\sqrt{s_{NN}} = 200$ GeV
 31 during the 2010 (Run10) and 2011 (Run11) RHIC runs, U + U collisions at $\sqrt{s_{NN}} = 193$
 32 GeV in 2012 (Run12). The minimum-bias (MB) trigger is defined as a coincidence between
 33 the two VPDs, a coincidence between the two ZDCs, and an online collision vertex cut.
 34 Moreover, a pile-up protection at the trigger level was applied for the data taking.

35 Events used in this analysis are required to have a valid collision vertex (primary vertex)
 36 within 30 cm of the TPC center along z direction (the direction along beam axis) to ensure
 37 uniform a TPC acceptance. Furthermore, the distance between the collision vertex along z
 38 direction constructed by the TPC (V_z^{TPC}) and the VPD (V_z^{VPD} , fast detector) is within 3
 39 cm to reject the event with wrong reconstructed TPC vertex from different bunch-crossing
 40 collisions. To reject the events from the beam hitting the beam pipe, vertex with a radial
 41 length less than 2 cm with respect to the beam pipe center is required. After event selection,
 42 A total of ~ 720 million Au + Au and ~ 270 million U + U minimum-bias events are finally
 43 used in this analysis. Table 1 lists the event selection criteria.

Table 1: Event selection in Au + Au collisions at 200 GeV and U + U collisions at 193 GeV.

Event Selection Criteria
$ V_r < 2$ cm
$ V_z^{TPC} < 30$ cm
$ V_z^{TPC} - V_z^{VPD} < 3$ cm

44 The centrality in Au + Au or U + U collisions is defined using the uncorrected charged
 45 particle density (dN_{ch}/dy). The primary tracks with $|\eta| \leq 0.5$, $dca \leq 3$ cm and $nHitsFit \geq$
 46 10 (number of hits used for track fitting) are used to calculate the dN_{ch}/dy . Furthermore, the
 47 dN_{ch}/dy is corrected for the V_z^{TPC} and luminosity dependence to account for the acceptance
 48 and efficiency changes on the measured dN_{ch}/dy . Then the dN_{ch}/dy is compared to a Monte
 49 Carlo (MC) Glauber calculation [1] to delineate the centrality bins, the equivalent number
 50 of binary nucleon + nucleon collisions (N_{bin} or N_{coll}) and the number of participants (N_{part})
 51 for nucleus + nucleus collisions. Table 2 and Table 3 list the $\langle N_{coll} \rangle$, $\langle N_{part} \rangle$ from Glauber
 52 model for each defined centrality bin in Au + Au collisions at $\sqrt{s_{NN}} = 200$ GeV, U + U
 53 collisions at $\sqrt{s_{NN}} = 193$ GeV, respectively. The 0-80% and finer centrality-bins within this
 54 range are used in this analysis, because the 80-100% centrality has significant trigger bias
 55 due to vertex inefficiency at low charged particle density.

Table 2: Centrality bins and corresponding $\langle N_{coll} \rangle$, $\langle N_{part} \rangle$ in Au + Au at 200 GeV.

Centrality	$\langle N_{coll} \rangle$	$\langle N_{part} \rangle$	Centrality	$\langle N_{coll} \rangle$	$\langle N_{part} \rangle$
0-5%	1048.11	349.64	5-10%	838.41	302.23
10-15%	663.04	256.76	15-20%	524.31	217.77
20-25%	411.86	183.75	25-30%	320.78	154.24
30-35%	246.95	128.30	35-40%	186.69	105.44
40-45%	138.71	85.48	45-50%	101.51	68.32
50-55%	72.79	53.86	55-60%	51.62	41.74
60-65%	35.64	31.62	65-70%	23.96	23.35
70-75%	15.98	16.96	75-80%	10.54	12.11

Table 3: Centrality bins and corresponding $\langle N_{coll} \rangle$, $\langle N_{part} \rangle$ in U + U at 193 GeV.

Centrality	$\langle N_{coll} \rangle$	$\langle N_{part} \rangle$	Centrality	$\langle N_{coll} \rangle$	$\langle N_{part} \rangle$
0-5%	1281.26	414.87	5-10%	1010.97	355.42
10-15%	798.53	300.92	15-20%	628.01	253.66
20-25%	490.60	212.84	25-30%	379.86	177.48
30-35%	290.31	146.78	35-40%	217.35	119.63
40-45%	160.03	96.34	45-50%	115.69	76.43
50-55%	81.76	59.55	55-60%	56.98	45.73
60-65%	38.36	34.01	65-70%	25.06	24.55
70-75%	16.28	17.46	75-80%	10.23	11.98

56 2 Electron Identification

57 The same electron identification technique is employed in both
 58 Au + Au collisions at 200 GeV and U + U collisions at 193 GeV.
 59 The detailed electron selection criteria in Au + Au collisions at
 60 200 GeV can be found in p3-p6 of PSN0636. The following three
 61 sub-sections are for U + U collisions at 193 GeV.

62 2.1 Track Selection

63 The interested electrons (including positrons if not specified) are mainly
 64 from the collision point or short-lived particle decays close to the collision
 65 point. Thus the primary tracks, including the primary vertex for the track
 66 fitting resulting in a better momentum resolution, are used in this analysis.
 67 The primary tracks are required to satisfy the following selection criteria:
 68 p_T is ≥ 0.2 GeV/c to ensure that the track can pass through the TPC;
 69 the Distance of Closest Approach (dca) to the primary vertex is ≤ 1 cm
 70 to reduce contributions from secondary decays; the number of hit points
 71 (nHitsFit) along the track is ≥ 20 (of a maximum of 45) to ensure good
 72 momentum resolution; the ratio of number of hit points along the track over
 73 the number of maximum possible points (nHitsPoss) is ≥ 0.52 to suppress
 74 the possibility of selecting duplicated short tracks from track splitting; the
 75 number of points used for calculating $\langle dE/dx \rangle$ (nHitsDedx) is ≥ 15 to ensure
 76 good dE/dx resolution; at last, the track is required to match with the TOF
 77 and restricted to $|\eta| \leq 1$.

78 2.2 Electron Identification Cuts

79 The electron candidates could be identified by combining the TPC and
 80 TOF. The TPC provides particle identification utilizing the dE/dx , because
 81 different particle species with the same momentum may have different dE/dx .
 82 However, in some momentum regions, the TPC can not identify different

Table 4: Electron candidates selection criteria in U + U collisions at 193 GeV.

Track Quality Cuts	Electron Identification Cuts
$0.2 \leq p_T \leq 30 \text{ GeV}/c$ $ \eta \leq 1$ $\text{nHitsFit} \geq 20$ $\text{nHitsFit}/\text{nHitsPoss} \geq 0.52$ $\text{nHitsDedx} \geq 15$ $\text{dca} \leq 1 \text{ cm}$	$p < 1 \text{ GeV}/c,$ $1.5625 \times (p - 0.2) - 2 - \mathbf{0.34} \leq n\sigma_e \leq 2 - \mathbf{0.34}$ $p \geq 1 \text{ GeV}/c,$ $-0.75 - \mathbf{0.34} \leq n\sigma_e \leq 2 - \mathbf{0.34}$ $ 1 - 1/\beta \leq 0.025$

83 particle species with very similar dE/dx (e.g. e/K at $p \approx 0.5 \text{ GeV}/c$, e/p
 84 at $p \approx 1 \text{ GeV}/c$). Different particle species with the same momentum have
 85 different velocities, thus the TOF with $<80 \text{ ps}$ time resolution can be used
 86 to identify different particle species in the dE/dx crossover regions by precise
 87 velocity information ($1/\beta = ct/l$). The normalized dE/dx , defined in Eq. 1,
 88 instead of dE/dx is used in this analysis. Where $\langle dE/dx \rangle^{\text{Mea.}}$ and $\langle dE/dx \rangle_e^{\text{Th.}}$
 89 represent measured and theoretical dE/dx , and $R_{dE/dx}$ is the STAR TPC
 90 dE/dx resolution (typically $\sim 8\%$).

$$n\sigma_e = \frac{1}{R_{dE/dx}} \log \frac{\langle dE/dx \rangle^{\text{Mea.}}}{\langle dE/dx \rangle_e^{\text{Th.}}} \quad (1)$$

91 By applying the TOF velocity cut, the slow hadrons are rejected from
 92 electrons in the dE/dx overlapping regions, as shown in Fig. 1. After the
 93 TOF velocity cut, the $n\sigma_e$ cut is applied to reject hadrons with almost the
 94 same velocity as electrons, as shown in Fig. 2. The electron sample is then
 95 extracted. A tachyon band is observed in the Fig. 1, that is because TOF hits
 96 from electrons originating from photon conversions in the material between
 97 the TPC and TOF leaving no trace in the TPC are randomly associated
 98 with TPC tracks especially in high-multiplicity collisions [2]. The random
 99 match could also result in some slow hadrons surviving the TOF velocity
 100 cut. Besides the random match, the secondary particles with inaccurate
 101 track length and flight time measurement may also survive the TOF velocity

cut. For those survived slow hadrons, if their dE/dx overlap with electrons, there is no way to reject them, as shown in Fig. 2. Thus the electron purity should be estimated, as discussed in Sec. 2.3. For the systematic uncertainty study from hadron contamination, it will be discussed in Sec. 6. Table. 4 lists the track selection criteria and electron identification cuts in U + U collisions at 193 GeV. The $n\sigma_e$ distribution of the pure electron sample is centered at -0.34 instead of 0 due to the imperfect TPC calibration, as shown in Fig. 5. Thus the $n\sigma_e$ cut is shift down 0.34 to account for this effect.

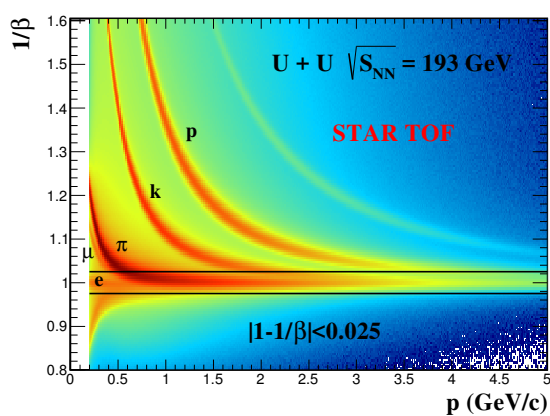


Figure 1: $1/\beta$ vs. particle momentum distribution.

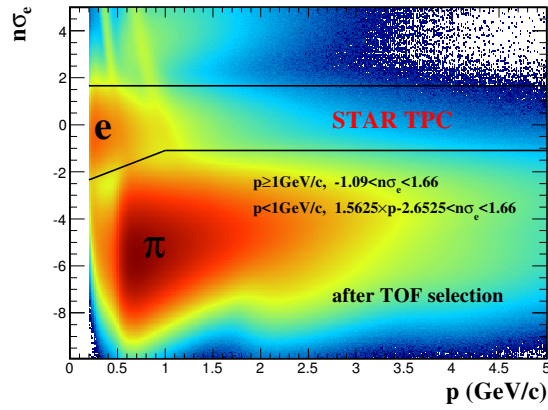


Figure 2: $n\sigma_e$ vs. particle momentum after the high velocity cut applied, as shown in Fig. 1.

2.3 Electron Purity

The pure hadron samples ($\pi/K/p$) are selected by combining tight m^2 and loose $n\sigma_{hadron}$ cuts. The selection criteria and $n\sigma_e$ distribution for each pure hadron sample are shown in Fig. 3. The pure electron sample is from the π^0 Dalitz decay and photon conversion. The invariant mass of the electron pair from photon conversion should be zero. However, the primary track, forced to originate from primary vertex, is used to reconstruct the electron pair invariant mass (see detailed procedure in Sec. 3). That will introduce an artificial opening angle between electron and positron resulting in a non-

zero invariant mass. The angle depends on the distance between the photon conversion point and the primary vertex. Thus the photons converting at different positions result in different invariant mass. The $M_{ee} < 0.015 \text{ GeV}/c^2$ is used to select the π^0 Dalitz decayed and photon conversion electrons with 148:1 (in minimum-bias collisions) signal-to-background ratio, shown in the left panel of Fig. 4. After subtracting the same sign electron pairs from the opposite sign electron pairs, shown in the right panel of Fig. 4, the pure electron sample is thus extracted, shown in Fig. 5. Due to the high charged particle density in U + U collisions at 193 GeV, it is likely to happen that two tracks with same charge and similar momentum are very closed to each other. The two tracks are very likely to be reconstructed into “one track” due to the finite hit position resolution, so called “merged track”. The pion is very abundant in U + U collisions at 193 GeV, thus the “merged π ” should be taken into account for the purity study. The “merged π ” could be selected using the same m^2 cut as normal π but with $n\sigma_\pi > 6$ (“merged π ” is with doubled dE/dx compared to a normal π). The $n\sigma_e$ distribution of each selected pure sample could be fitted by Gaussian function in each fine p_T bin. The mean and sigma of the $n\sigma_e$ distribution as a function of momentum for each pure sample in minimum-bias collisions are shown in Fig. 6. The electron purity is then estimated based on multi-Gaussian fitting to the $n\sigma_e$ distribution after applying TOF velocity cut. The mean and width of each component is constrained by the values in Fig. 6 when multi-Gaussian fitting is performed. Figure 7 shows examples of the multi-Gaussian fitting in three specific momentum regions. In the dE/dx overlap regions (e.g. e/K at $p \approx 0.5 \text{ GeV}/c$, e/p at $p \approx 1 \text{ GeV}/c$), the multi-Gaussian fitting is not reliable. An exponential function is employed to extrapolate the hadron particle yields in the overlapping regions as shown in the left panel of Fig. 8. The hadron yields are then constrained, just leaving the electron yield as a free parameter, in the multi-Gaussian function for refitting. The electron yield from the second-round multi-Gaussian fitting is extracted to check the fit reliability, shown

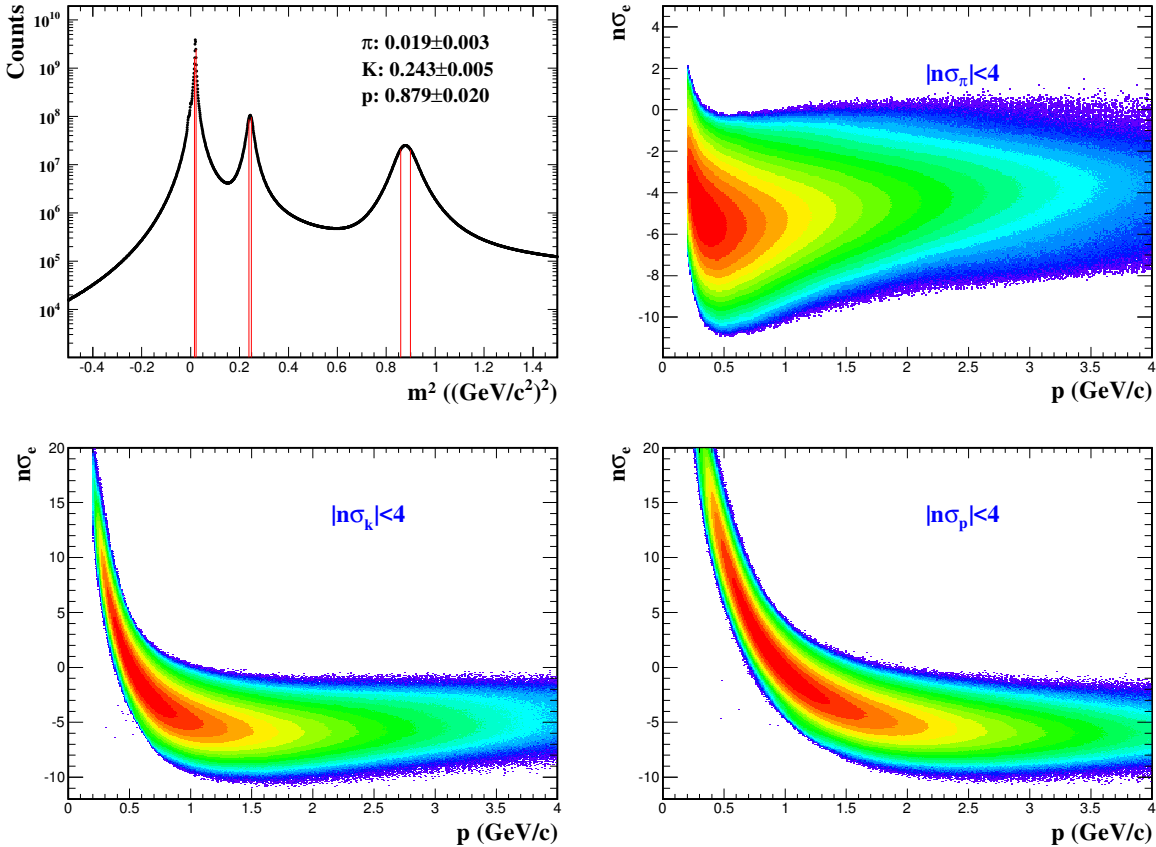


Figure 3: The selection criteria and $n\sigma_e$ distribution as a function of momentum for each pure hadron sample in U + U 193 GeV minimum-bias collisions. (Top Left) m^2 distribution of different particle species and pure hadron m^2 selection criteria. (Top Right) Pure pion sample. (Bottom Left) Pure kaon sample. (Bottom Right) Pure proton sample.

149 in the right panel of Fig. 8. The electron purity difference between these
 150 two-round fittings is taken as the systematic uncertainty. Figure 9 shows the
 151 electron purity (overall at $\sim 95\%$) in U + U minimum-bias collisions at 193
 152 GeV.

153 3 Pair Reconstruction and Background Subtraction

154 The same technique is employed in both Au + Au collisions at
 155 200 GeV and U + U collisions at 193 GeV. The detailed foreground
 156 and background reconstruction in Au + Au collisions at 200 GeV

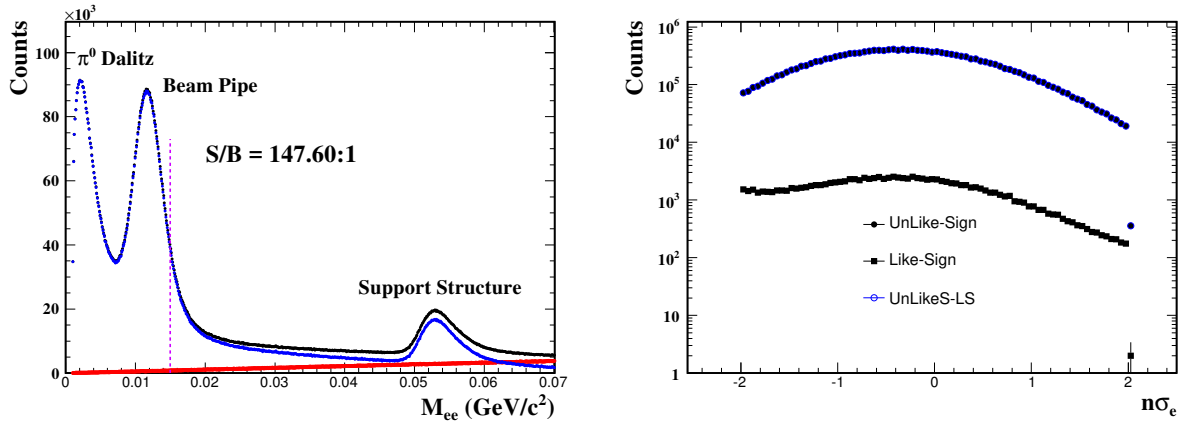


Figure 4: The selection criteria and $n\sigma_e$ distribution of pure electron sample in U + U minimum-bias collisions at 193 GeV. (Left) The invariant mass distribution of π^0 Dalitz decay and photon conversion electron pairs. (Right) The $n\sigma_e$ distribution of π^0 Dalitz decay and photon conversion electrons.

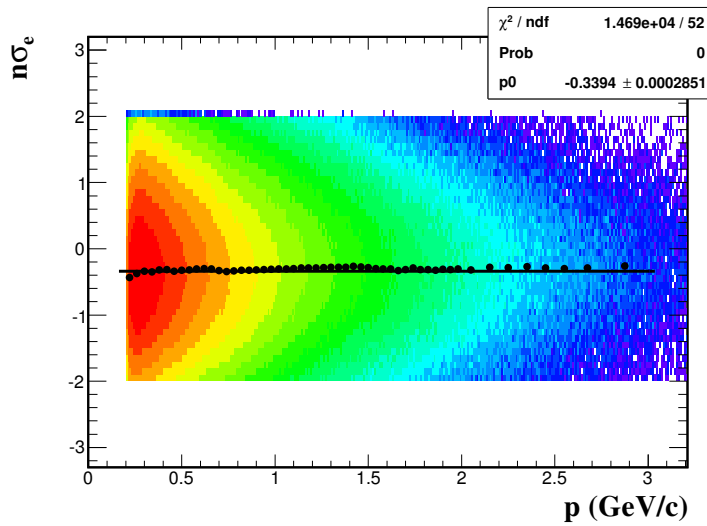


Figure 5: The $n\sigma_e$ distribution of pure electron sample as a function of momentum in U + U minimum-bias collisions at 193 GeV. The mean of the $n\sigma_e$, shown as black dots, is shift to -0.34 due to imperfect TPC dE/dx calibration.

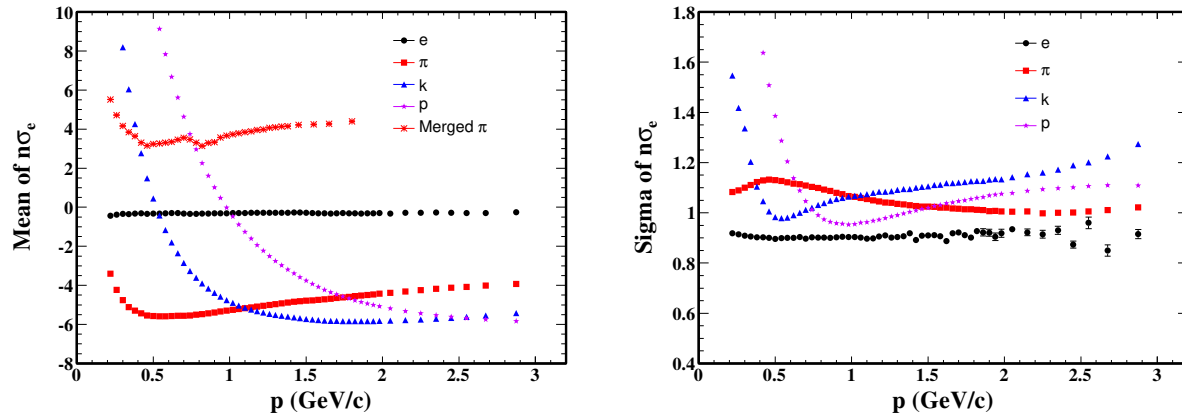


Figure 6: The mean (Left) and sigma (Right) of the $n\sigma_e$ for each pure particle sample as a function of momentum in U + U 193 GeV minimum-bias collisions.

157 can be found in p6-p15 of PSN0636. The Sec. 3.1, Sec. 3.2, and
158 Sec. 3.3 are for U + U collisions at 193 GeV.

159 The foreground (also called unlike-sign pairs, N_{+-} , including signal and
160 background) is reconstructed by combining the electron and positron candi-
161 dates in the same event. The invariant mass (M_{ee}) of the electron pairs are
162 calculated by Eq. 2,

$$M_{ee} = \sqrt{(E_+ + E_-)^2 - (\vec{p}_+ + \vec{p}_-)^2} \quad (2)$$

163 where $E_{+-} = \sqrt{m_e^2 + \vec{p}_{+-}^2}$, $m_e = 0.511 \text{ MeV}/c^2$ and \vec{p}_{+-} are measured by
164 the TPC. The signals come from the Drell-Yan production, quarkonia decay,
165 QGP thermal radiation, heavy flavor semi-leptonic decay, vector mesons in-
166 medium decay and long-lived hadron decays. The background sources include
167 the combinatorial background, correlated background and photon conver-
168 sions. The combinatorial background comes from uncorrelated electron and
169 positron pairing while the correlated background comes from correlated elec-
170 tron and positron pairing; for example, pairs from Dalitz decay followed by a
171 conversion of the decayed photon (e.g. $\pi^0 \rightarrow \gamma + e^+ + e^- \rightarrow e^+ + e^- + e^+ + e^-$)
172 or jets (e.g. electron and positron are from same-jet fragmentation or back-
173 to-back di-jet fragmentation). The photon conversion background is from the

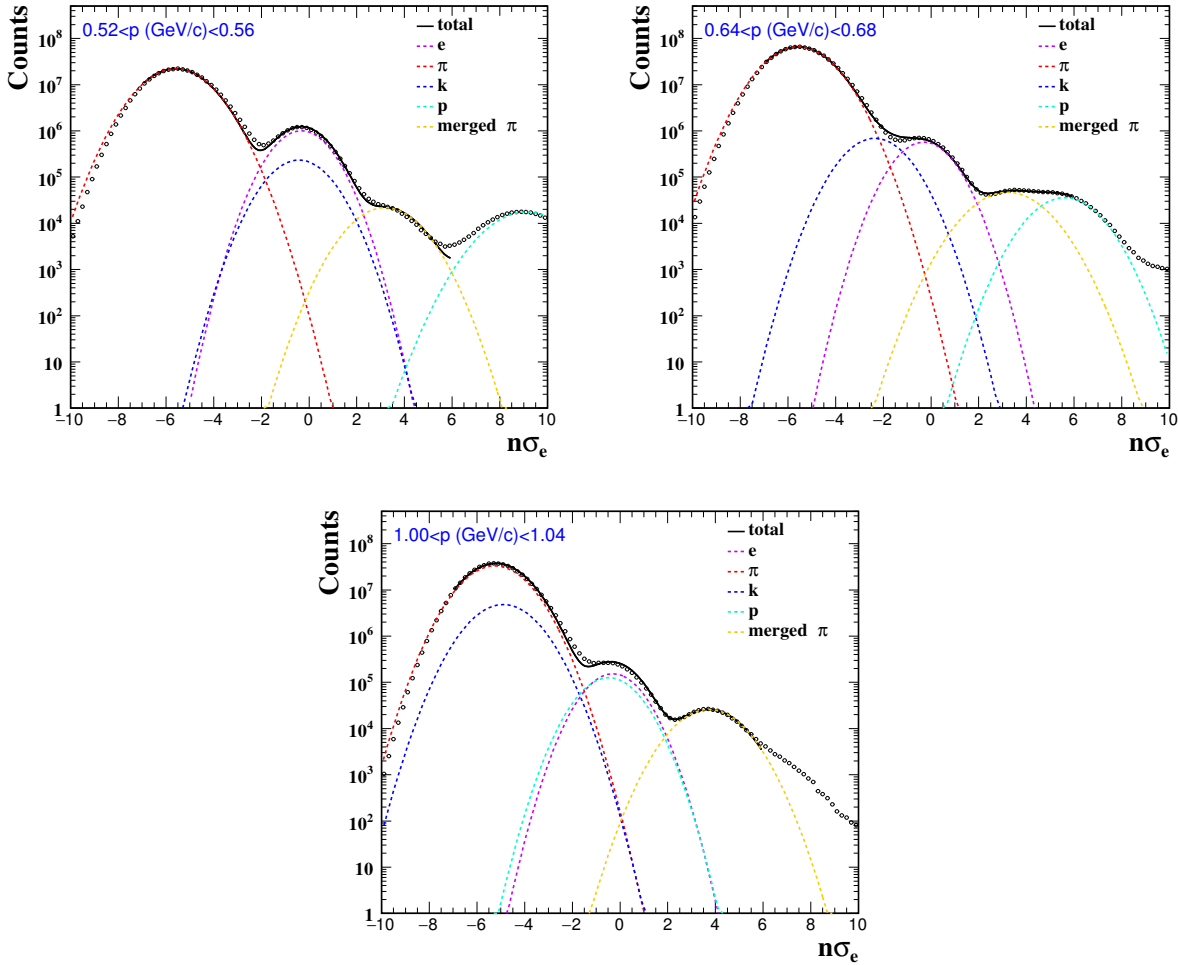


Figure 7: The $n\sigma_e$ distribution after the TOF velocity cut and the multi-Gaussian fit results in three specific momentum bins.

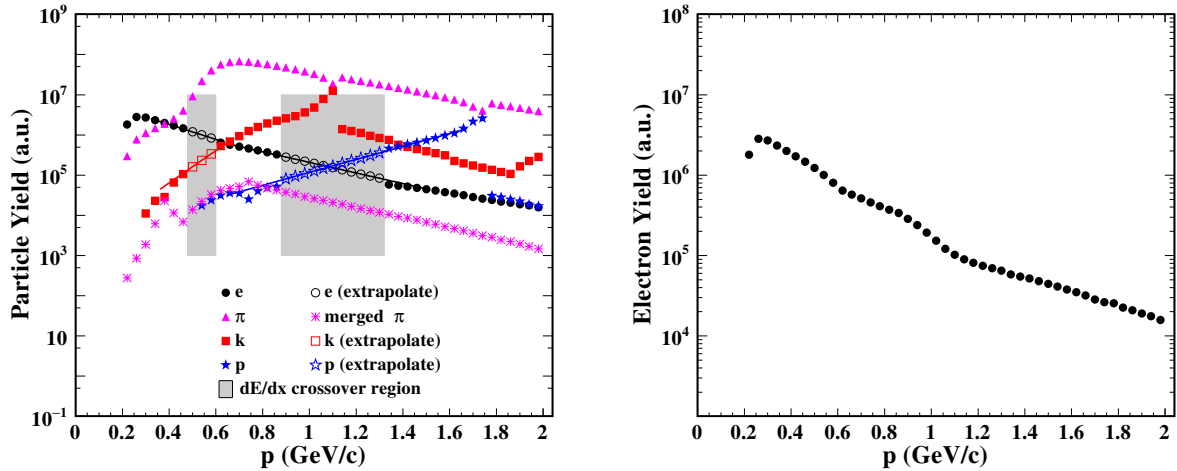


Figure 8: (Left) The yields (solid markers) for different particle species extracted from first-round multi-Gaussian fitting as a function of momentum. The gray areas (left: e/K , right: e/p) depict the dE/dx crossover regions. The solid lines are the exponential fits for extrapolating the hadron yields (open markers) in the crossover regions. (Right) The electron yields (the only free parameter) from the second-round multi-Gaussian fitting to check the fitting reliability.

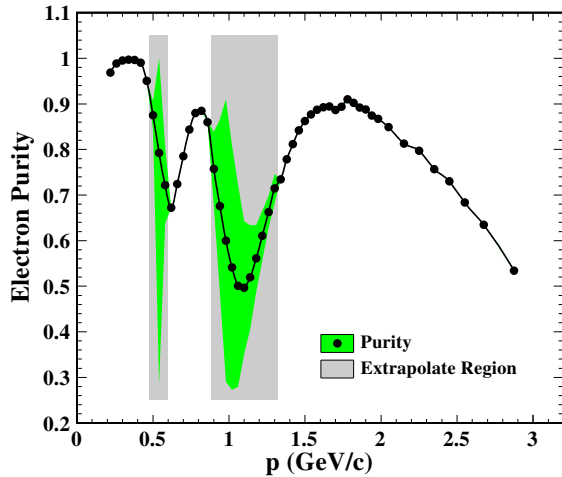


Figure 9: The electron purity in $U + U$ minimum-bias collisions at 193 GeV, the green band represents the systematic uncertainties.

¹⁷⁴ photon interacting with the detector material and converting into an electron-
¹⁷⁵ positron pair. The reconstruction and subtraction of these three background
¹⁷⁶ sources are discussed in following sections.

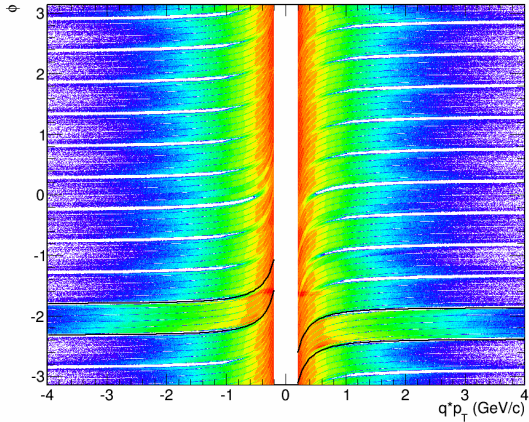


Figure 10: The ϕ vs. p_T distributions for electron and positron candidates. The blank strips are caused by the read-out sector boundaries. The bad TPC sector (sector 7, in positive η region) is constrained by the black solid lines.

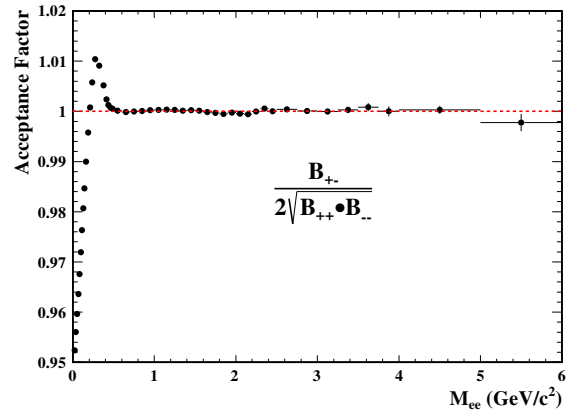


Figure 11: The 1-D acceptance correction factor as a function of M_{ee} in Run12 U + U minimum-bias collisions at 193 GeV.

¹⁷⁷ 3.1 Like-sign Technique

¹⁷⁸ The like-sign technique, combining same charge sign electrons into pairs
¹⁷⁹ in the same event (N_{++} and N_{--}), is used to account for the combinatorial
¹⁸⁰ and correlated backgrounds. The geometric mean of the like-sign pairs
¹⁸¹ $2\sqrt{N_{++} \cdot N_{--}}$, demonstrated in [3], can fully describe the background in the
¹⁸² foreground when the e^+ and e^- are produced in statistically independent
¹⁸³ pairs. The geometric mean is consistently used in the same-event like-sign
¹⁸⁴ background reconstruction.

¹⁸⁵ The electrons and positrons are bended into opposite directions owing to
¹⁸⁶ the magnetic field. The ϕ versus p_T of the identified electron and positron
¹⁸⁷ candidates is shown in Fig. 10. The blank strips along the ϕ direction are

caused by the TPC read-out sector boundaries. There is one TPC sector (sector 7, in positive η region) with dE/dx calibration issue in Run12 U + U collisions, depicted by the black solid lines in Fig. 10. Thus all the tracks passing through this TPC sector are consistently rejected in this analysis. Due to the magnetic field and the TPC de-active areas (read-out sector boundaries, acceptance holes), the acceptances for the unlike-sign and like-sign pairs are different. The mixed-event technique, discussed in Sec. 3.2, is employed to correct for this effect. The correction factor is calculated by the ratio of the mixed-event unlike-sign and like-sign distribution in each (M_{ee}, p_T^{ee}) bin and applied in 2-dimension (2-D). The final same-event like-sign background used is calculated by the Eq. 3,

$$N_{++\&--}^{corr} = 2\sqrt{N_{++}(M, p_T) \cdot N_{--}(M, p_T)} \times \frac{B_{+-}(M, p_T)}{2\sqrt{B_{++}(M, p_T) \cdot B_{--}(M, p_T)}} \quad (3)$$

where N_{++} , N_{--} , B_{++} , and B_{--} represent the distribution of like-sign from the same-event and mixed-event, respectively. B_{+-} represents the distribution of unlike-sign from the mixed-event. $N_{++\&--}^{corr}$ denotes the acceptance-corrected like-sign background from the same-event. Figure 11 shows the 1-D acceptance correction factor as a function of M_{ee} in Run12 U + U minimum-bias collisions at 193 GeV.

3.2 Mixed-Event Technique

The like-sign technique, discussed in Sec. 3.1, is taken as the best estimation for the combinatorial and correlated backgrounds. However, it is limited to the statistics. The mixed-event technique, combining the electrons and positrons from different events with similar characteristics, is used to reproduce the combinatorial background with improved statistical precision. The data sample is divided into different event pools according to the following event level properties: z position of collision vertex, reference multiplicity, and event plane angle. The collision vertex position and reference multi-

plicity ensure that the same event pool has similar detector acceptance and efficiency. The event plane angle ensures the same event pool has similar momentum phase space alignment, and further guaranteed by the multiplicity assortment to ensure the events have similar momentum phase space distribution. The second-order event plane angle [4, 5] is used to sort the events. The z vertex position, from -30 cm to +30 cm, is divided into 10 equidistant bins. The reference multiplicity is divided into 16 bins (0 - 80%, discussed in Sec. 1) according to the official StRefMult package provided by STAR. The event plane angle Ψ is divided into 24 equidistant bins. This granularity of the event pools is determined by the same procedure discussed in [2]. Each event pool holds 100 events at maximum, and one event in the event pool is randomly updated when the pool is full.

The mixed-event background must be normalized to the acceptance corrected same-event like-sign background. The mixed-event technique can not reproduce the correlated background, thus the normalization factor should be determined in a kinematic region where the same-event like-sign correlated background is negligible. Once the kinematic region selected, the normalization factor and the normalized combinatorial background (B_{+-}^{comb}) are calculated via the same method in [3] and also shown in Eq. 4

$$\begin{aligned}
 A_+ &= \frac{\int_{N.R.} N_{++}(M, p_T) dM dp_T}{\int_{N.R.} B_{++}(M, p_T) dM dp_T} \\
 A_- &= \frac{\int_{N.R.} N_{--}(M, p_T) dM dp_T}{\int_{N.R.} B_{--}(M, p_T) dM dp_T} \\
 B_{++}^{norm} &= \int_0^\infty A_+ B_{++}(M, p_T) dM dp_T \\
 B_{--}^{norm} &= \int_0^\infty A_- B_{--}(M, p_T) dM dp_T \\
 B_{+-}^{comb}(M, p_T) &= \frac{2\sqrt{B_{++}^{norm} B_{--}^{norm}}}{\int_0^\infty B_{+-}(M, p_T) dM dp_T} B_{+-}(M, p_T)
 \end{aligned} \tag{4}$$

where N.R. represents the normalization region, A_{+-} is the like-sign normalization factor in N.R., $B_{++/--}^{norm}$ is the normalized mixed-event like-sign

statistics and B_{+-}^{comb} is the normalized mixed-event unlike-sign distribution. Unfortunately the mixed-event technique, working in Au + Au at 200 GeV, does not work in U + U at 193 GeV. There is no flat kinematic region found to do the normalization, as shown in Fig. 12. To check the possible effect of missing TPC sector 7 on the mixed-event distribution in U + U collisions, we artificially removed this TPC sector (shown in Fig. 13) in Au + Au collisions as we did in the U + U collisions, but we can still find a flat kinematic region to perform the normalization for Au + Au collisions, as shown in Fig. 14. Thus, the failure of mixed-event technique in U + U collisions may be related to the asymmetric Uranium geometry compared to the symmetric Gold geometry, shown in Fig. 15. The same-event like-sign technique is finally used to reconstruct the background in U + U collisions at 193 GeV. **For the very low p_T dielectron analysis, due to the good signal background ratio, the same-event like-sign technique is also consistently used to reproduce the background in Au + Au collisions at 200 GeV.**

3.3 Photon Conversion Removal

The photon conversion electron pairs are removed from the foreground using the ϕ_V cut method which is similar to that used by the PHENIX Collaboration [3]. The opening angle between the electron and positron from the photon conversion should be 0, and the electron and positron are bent only in the plane perpendicular the magnetic field direction which is along the beam axis z in STAR. The definitions of the unit vector and ϕ_V angle are shown in the following Eq. 5:

$$\begin{aligned}\hat{u} &= \frac{\vec{p}_+ + \vec{p}_-}{|\vec{p}_+ + \vec{p}_-|}, \quad \hat{v} = \vec{p}_+ \times \vec{p}_- \\ \hat{w} &= \hat{u} \times \hat{v}, \quad \hat{w}_c = \hat{u} \times \hat{z} \\ \cos\phi_V &= \frac{\hat{w}}{|\hat{w}|} \cdot \frac{\hat{w}_c}{|\hat{w}_c|}\end{aligned}\tag{5}$$

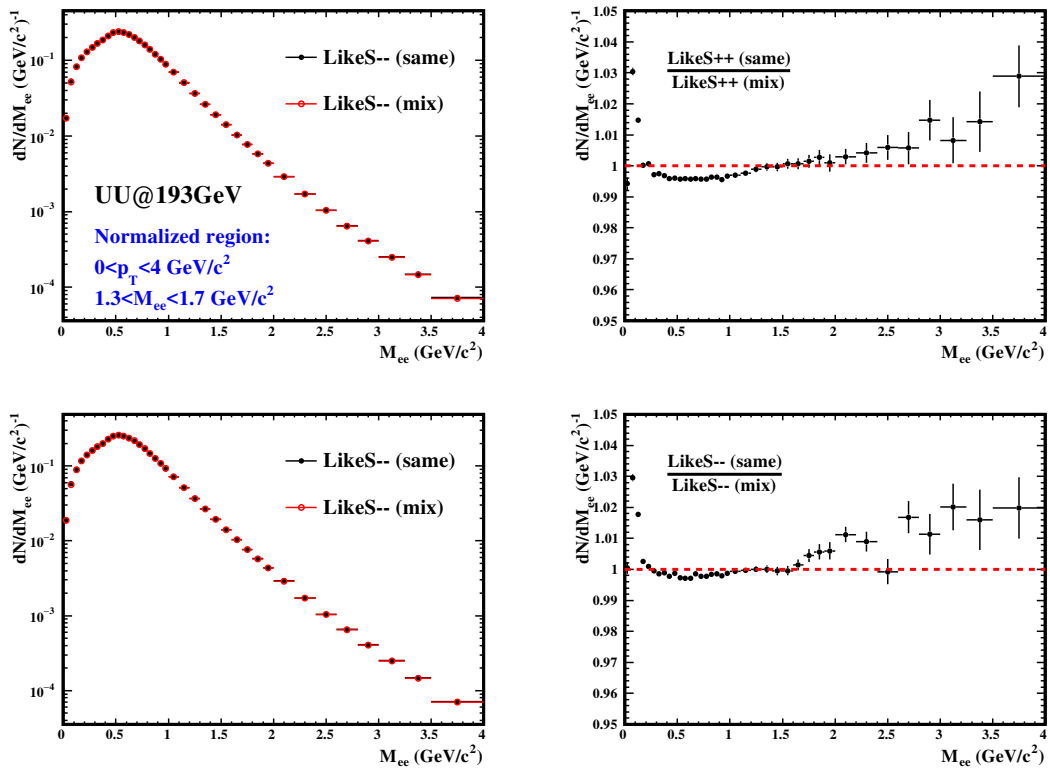


Figure 12: The same-event and mixed-event like-sign distributions in 0-80% U+U collisions and corresponding ratios. There is no flat kinematic region to do the mixed-event normalization.

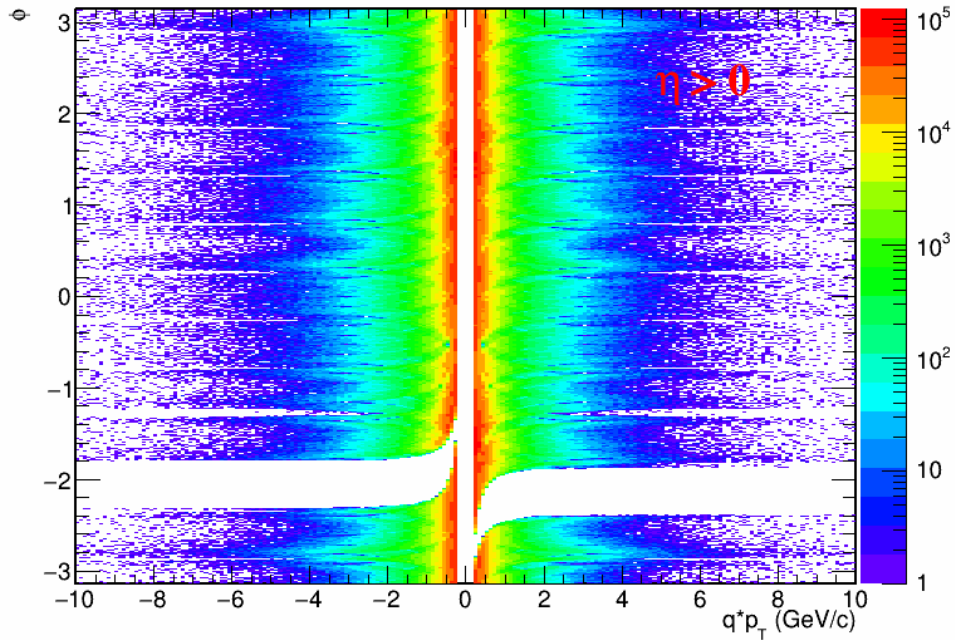


Figure 13: The ϕ vs. p_T distributions for electron and positron candidates for $\eta > 0$ in AuAu collisions.

To illustrate the ϕ_V angle, a little more explanation is added here. Plane

A is defined by mother particle momentum direction and beam axis direction, while plane B is defined by the daughter electron, positron momentum directions. The angle between plane A and plane B is defined as ϕ ($0^\circ \leq \phi \leq 90^\circ$). According to Eq. 5, $\phi_V = 90^\circ - / + \phi$. For electron and positron from the photon conversion, $\phi = 90^\circ$, thus the ϕ_V angle is zero or π . A fixed order between electron and positron is used to calculate the ϕ_V in this analysis for avoiding $\phi_V = \pi$. There is no preferred orientation for combinatorial electron and positron pairs, and only very weak dependence for electron and positron pairs from hadron decays. Figure 16 shows the ϕ_V angle as a function of invariant mass in U + U minimum-bias collisions at 193 GeV. The blue solid curve ($\phi_V(M_{ee}) = 0.84326 * e^{-49.4819 * M_{ee}} - 0.996609 * M_{ee} + 0.19801$) depicts the mass dependent ϕ_V cut employed to remove the photon conversion electron pairs. Figure 17 shows the invariant mass distribution of the

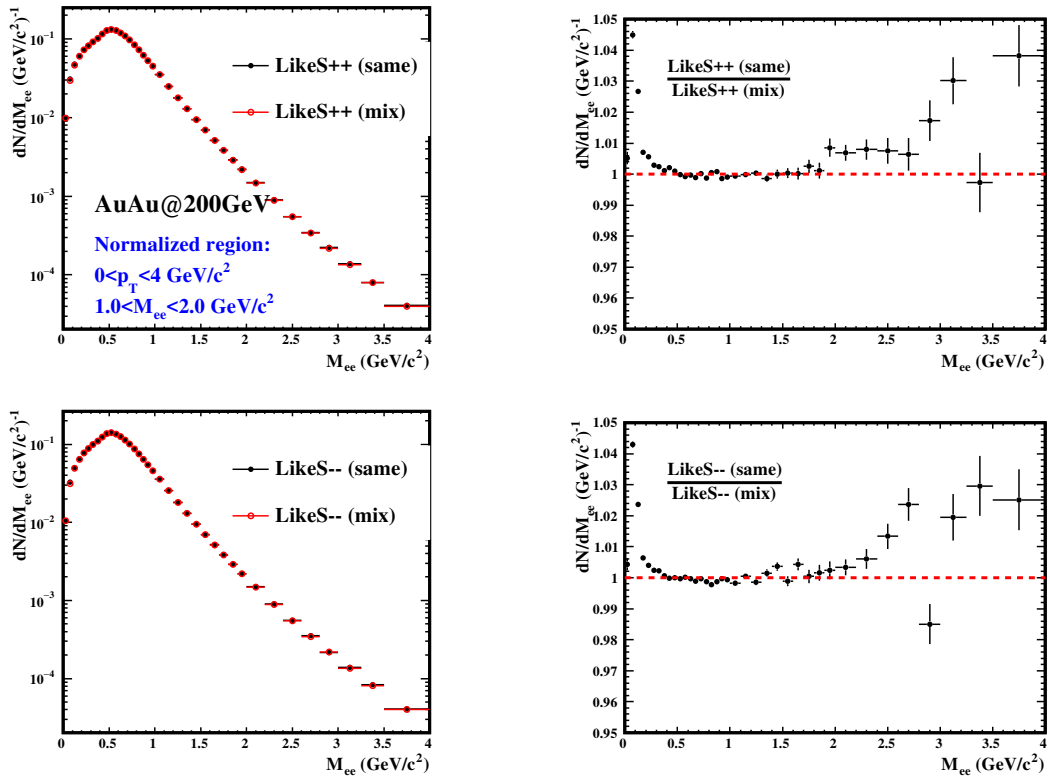


Figure 14: The same-event and mixed-event like-sign distributions in 0-80% Au+Au collisions and corresponding ratios without TPC sector 7. A flat kinematic region can be found to do the mixed-event normalization.

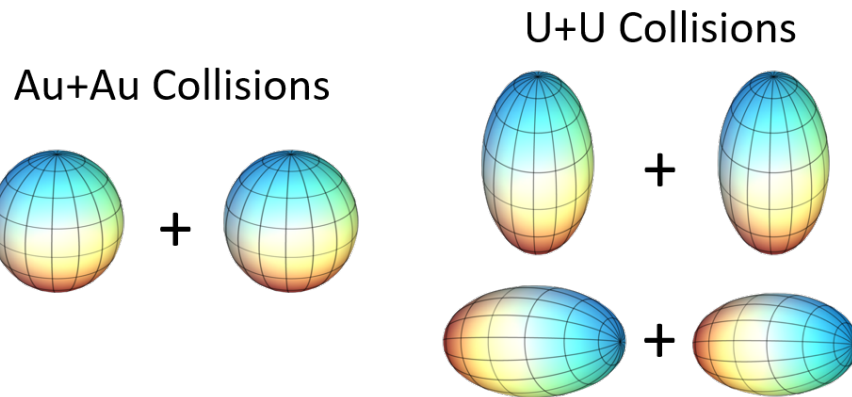


Figure 15: The spherical Gold nuclei (Left) and the ellipsoidal Uranium nuclei (Right).

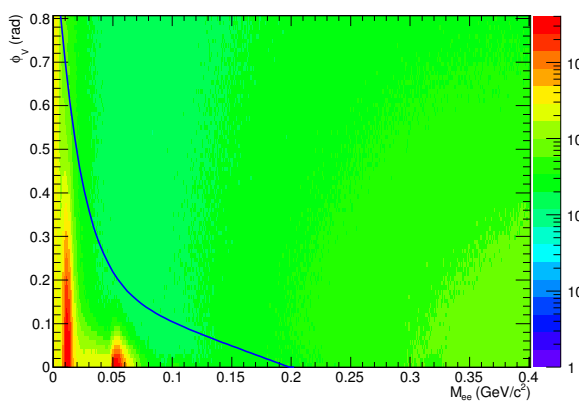


Figure 16: The ϕ_V angle vs. invariant mass distribution in Run12 U + U minimum-bias collisions at 193 GeV. The blue solid curve depicts the mass dependent ϕ_V cut employed to remove the photon conversion electron pairs.

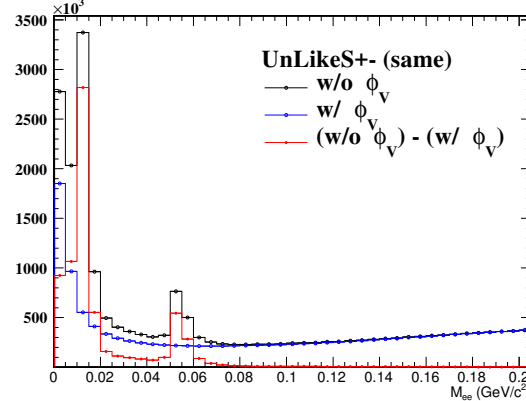


Figure 17: Red: the invariant mass distribution of the photon conversion electron pairs. Black: the unlike-sign distribution without ϕ_V cut. Blue: the unlike-sign distribution with ϕ_V cut.

272 photon conversion electron pairs (red curve). As mentioned before, the dif-
 273 ferent invariant mass peaks depict that the conversion electron pairs are from
 274 different materials. The mass shifted from zero is because the electrons are
 275 assumed to originate from the primary vertex during the final track recon-
 276 struction. Therefore, the two main peaks (for the red histogram) from low to
 277 high mass correspond to the conversion from the beam pipe and inner cone
 278 support structure, respectively.

279 3.4 Raw Signals

280 The background, in this analysis, is subtracted by the same-event like-sign
 281 technique. The same-event like-sign distribution is firstly corrected for the
 282 acceptance and then subtracted from the inclusive unlike-sign (foreground)
 283 distribution. The invariant mass distribution of signal pairs before detector
 284 efficiency losses correction (raw signal) is thus obtained. The upper panel
 285 of Fig. 18 shows the invariant mass distributions of foreground (black dots),
 286 background (black line) and raw signal (blue dots), while the bottom panel
 287 shows the signal-to-background ratio in U + U minimum-bias collisions at

²⁸⁸ $\sqrt{s_{NN}} = 193$ GeV. The raw spectra in different p_T bins from various U +
²⁸⁹ U centrality classes are shown in Fig. 19, 20, 21, and 22. The raw spectra
²⁹⁰ of p_T differentials in Run10 Au + Au collisions are shown in Fig. 23, 24, 25,
²⁹¹ and 26, while that in Run11 Au + Au collisions are shown in Fig. 27, 28, 29,
²⁹² and 30.

²⁹³ 4 Efficiency and Acceptance Corrections

²⁹⁴ To obtain the real invariant mass spectrum of dielectron within STAR
²⁹⁵ acceptance ($p_T^e \geq 0.2$ GeV/c, $|\eta_e| \leq 1$, $|Y_{ee}| \leq 1$), the raw spectrum should be
²⁹⁶ corrected for the efficiency losses. The pair efficiency within STAR acceptance
²⁹⁷ is evaluated by folding the single track efficiency. To measure the dielectron
²⁹⁸ excess yield and study the medium properties, the dielectron excess spectrum
²⁹⁹ (dielectron invariant mass spectrum with hadronic contributions except ρ -
³⁰⁰ meson subtracted, see details in Sec. 5) is needed to be corrected for the
³⁰¹ detector acceptance.

³⁰² 4.1 Single Track Efficiency

³⁰³ The single track efficiency losses are caused by the detector inefficiency
³⁰⁴ and electron identification cuts. The detector efficiency includes the TPC
³⁰⁵ tracking efficiency (ε_{TPC}), nHitsDedx cut efficiency ($\varepsilon_{nHitsDedx}$) and the TOF
³⁰⁶ matching efficiency (ε_{TOF}). The electron identification cut efficiency (ε_{eID})
³⁰⁷ includes the efficiencies of TOF velocity and the dE/dx selection cuts. So
³⁰⁸ the single track efficiency can be derived by the Eq. 6

$$\varepsilon_e = \varepsilon_{TPC} \times \varepsilon_{nHitsDedx} \times \varepsilon_{TOF} \times \varepsilon_{eID} \quad (6)$$

³⁰⁹ The detailed single track efficiency in Au + Au collisions at
³¹⁰ 200 GeV can be found in p18-p25 (0.4.1 Single track efficiency)
³¹¹ of PSN0636

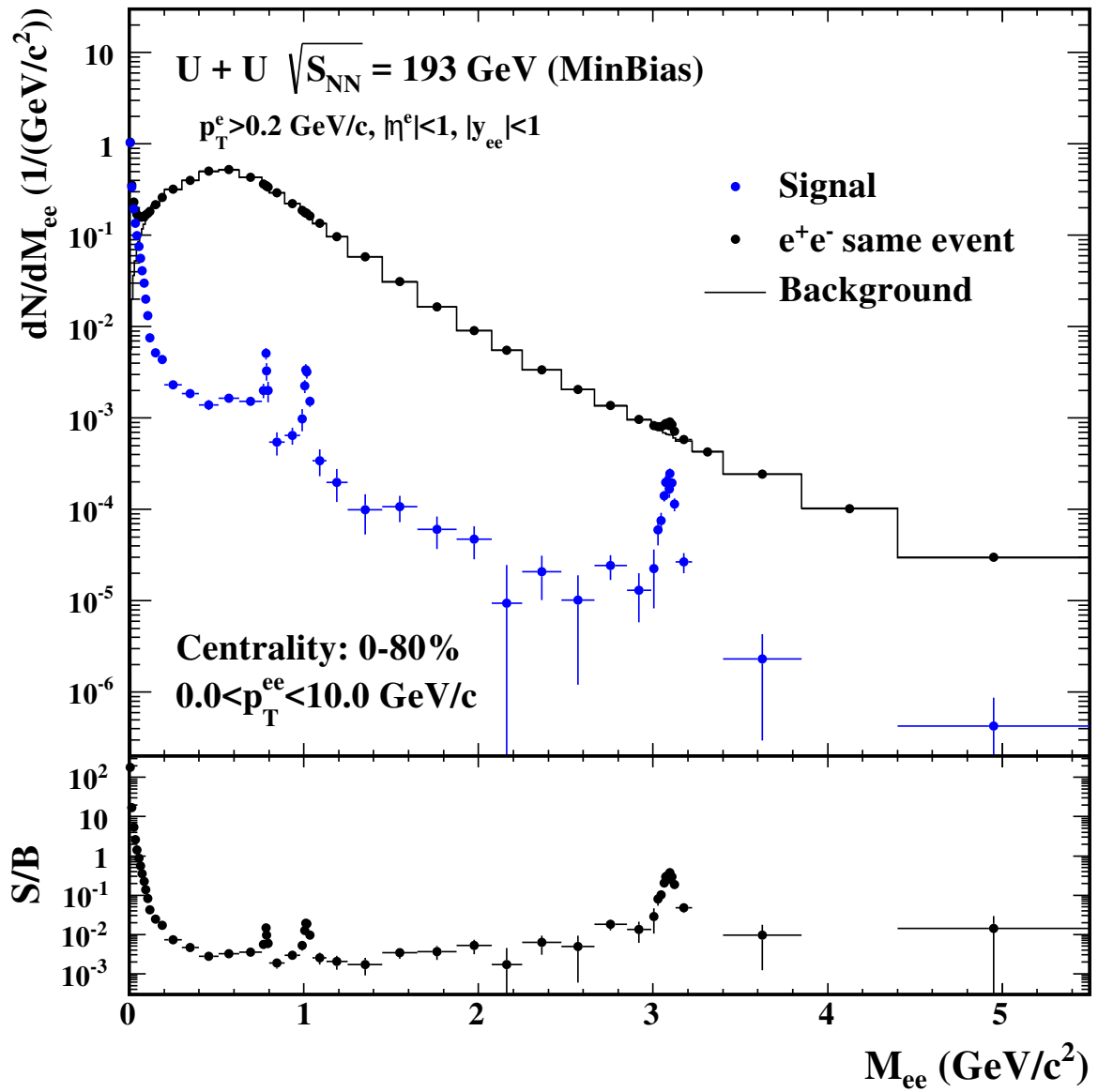


Figure 18: (Top) The invariant mass distributions of raw signal (blue dots), foreground (black dots) and background (black line). (Bottom) The signal-to-background ratio in $U + U$ minimum-bias collisions at $\sqrt{s_{NN}} = 193 \text{ GeV}$.

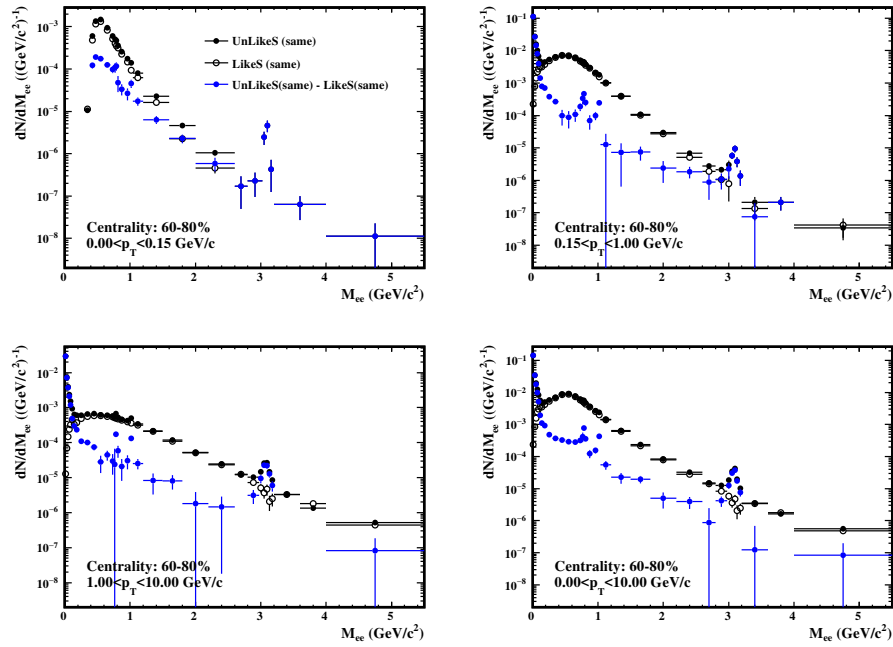


Figure 19: The invariant mass distributions of raw signal (blue dots), foreground (black dots) and background (black open circles) in $U + U$ 60-80% collisions at $\sqrt{s_{NN}} = 193$ GeV.

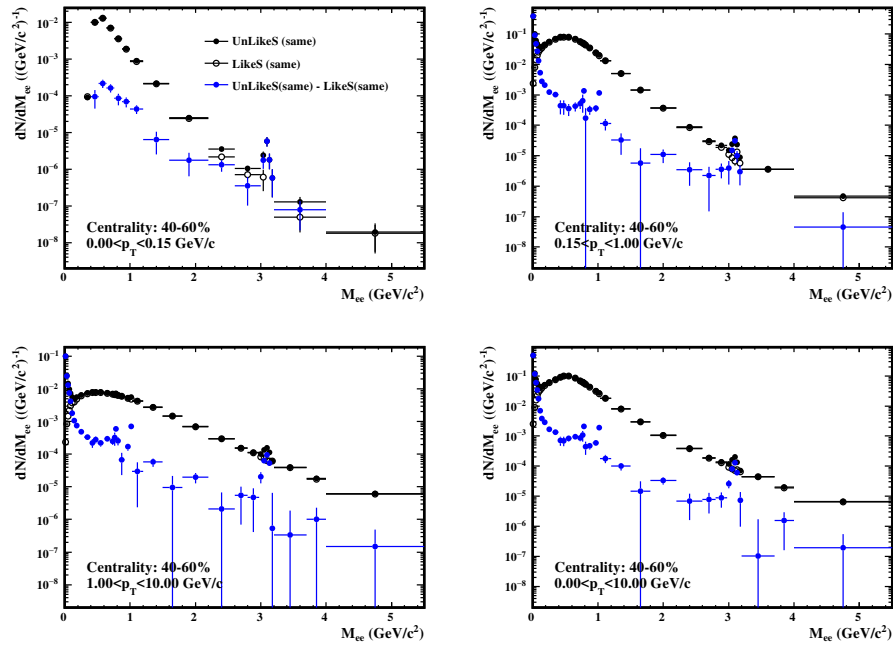
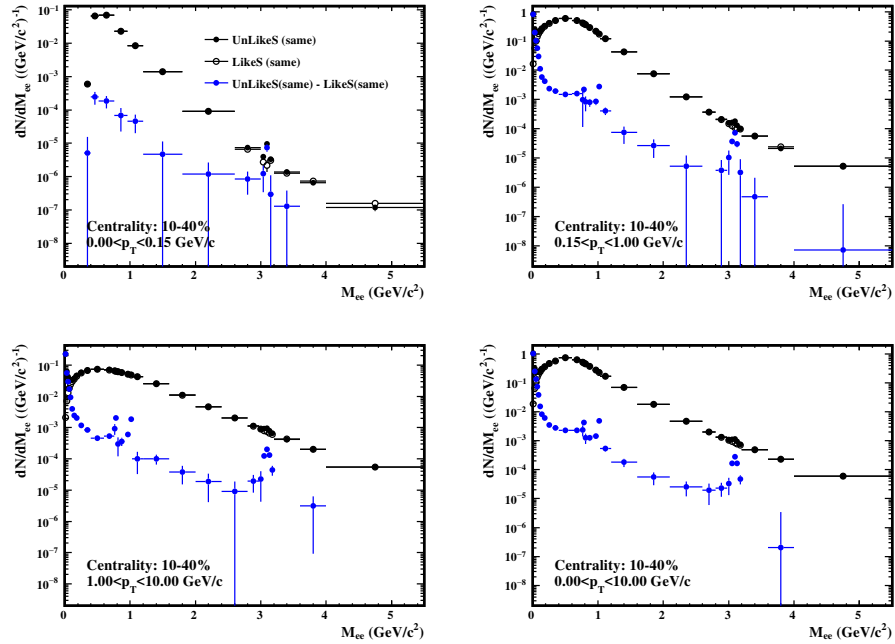
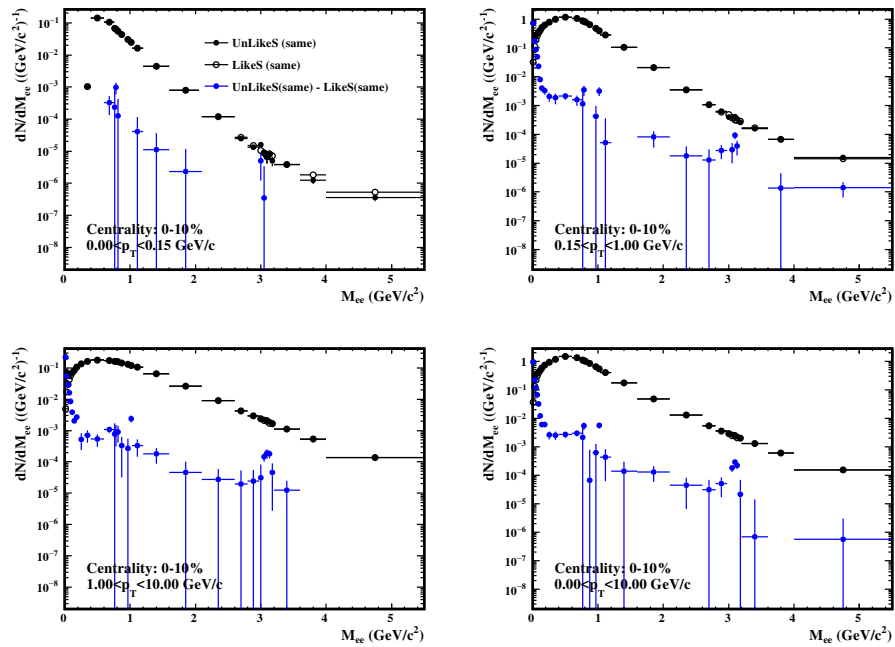


Figure 20: 40-60% $U + U$ collisions at $\sqrt{s_{NN}} = 193$ GeV.

Figure 21: 10-40% U + U collisions at $\sqrt{s_{NN}} = 193$ GeV.Figure 22: 0-10% U + U collisions at $\sqrt{s_{NN}} = 193$ GeV.

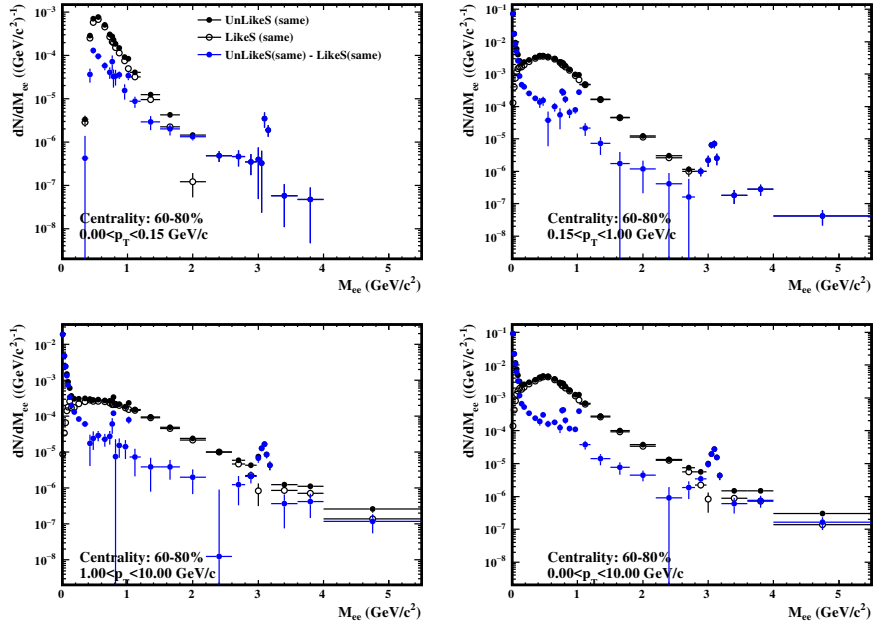


Figure 23: The invariant mass distributions of raw signal (blue dots), foreground (black dots) and background (black open circles) in Run10 Au + Au 60-80% collisions at $\sqrt{s_{NN}} = 200 \text{ GeV}$.

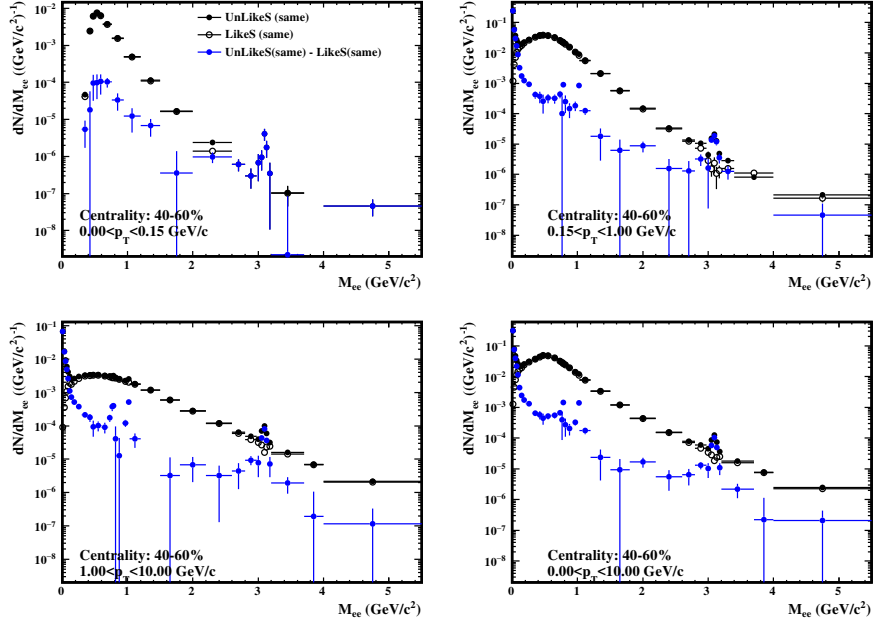
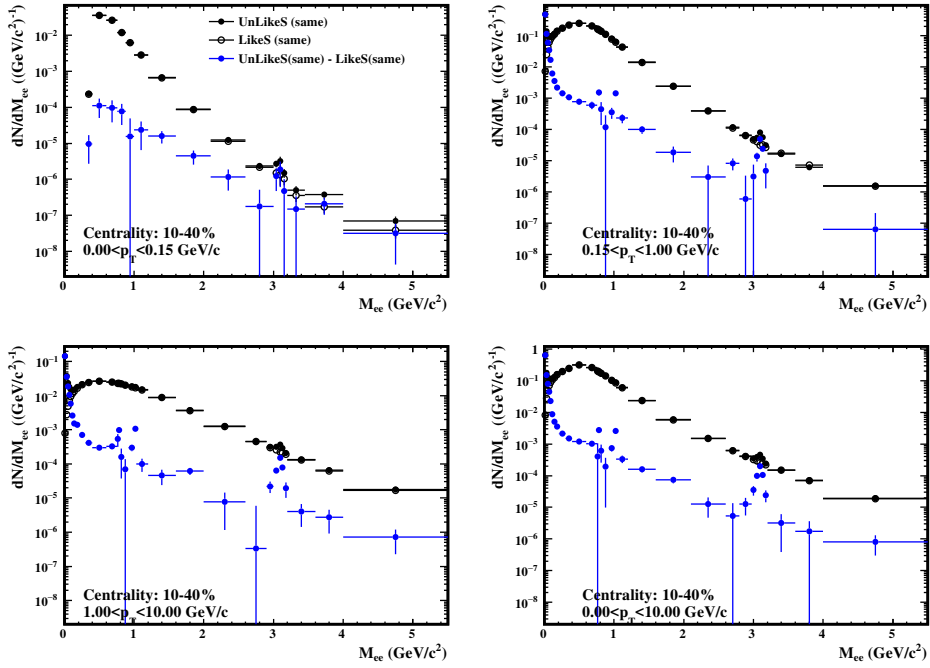
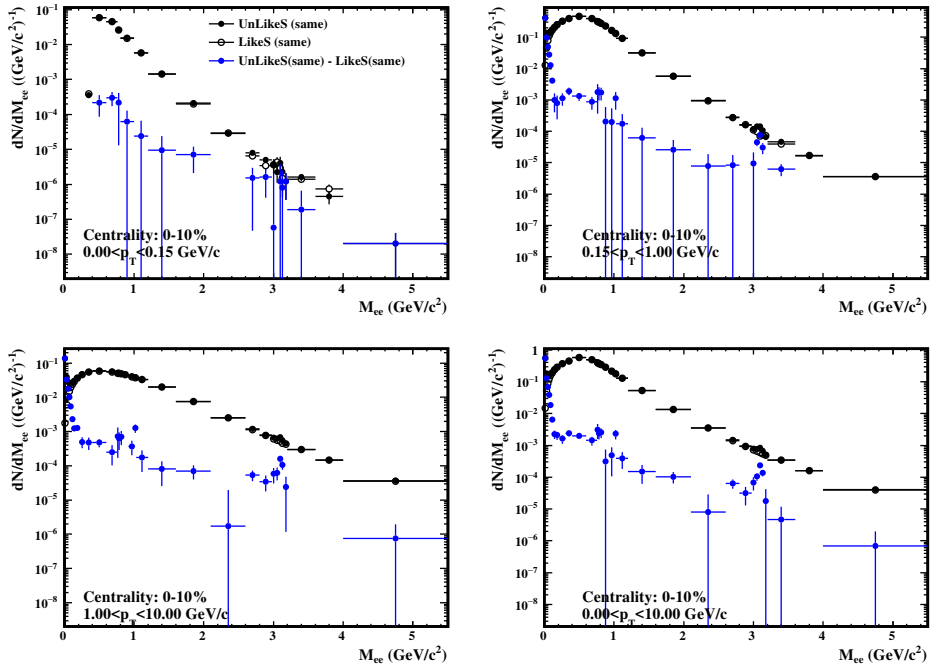


Figure 24: Run10 40-60% central Au + Au collisions at $\sqrt{s_{NN}} = 200 \text{ GeV}$.

Figure 25: Run10 10-40% central Au + Au collisions at $\sqrt{s_{NN}} = 200$ GeV.Figure 26: Run10 0-10% central Au + Au collisions at $\sqrt{s_{NN}} = 200$ GeV.

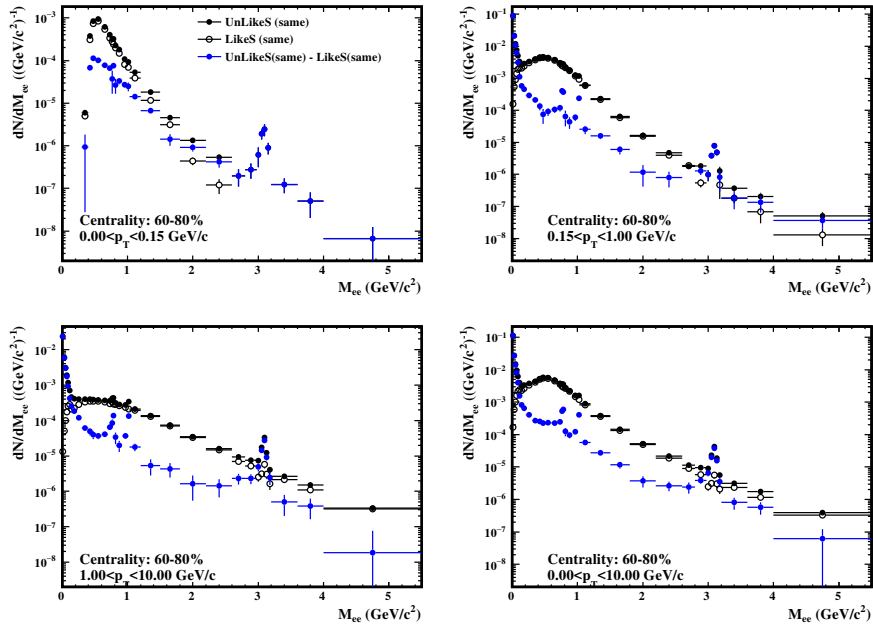


Figure 27: The invariant mass distributions of raw signal (blue dots), foreground (black dots) and background (black open circles) in Run11 Au + Au 60-80% collisions at $\sqrt{s_{NN}} = 200$ GeV.

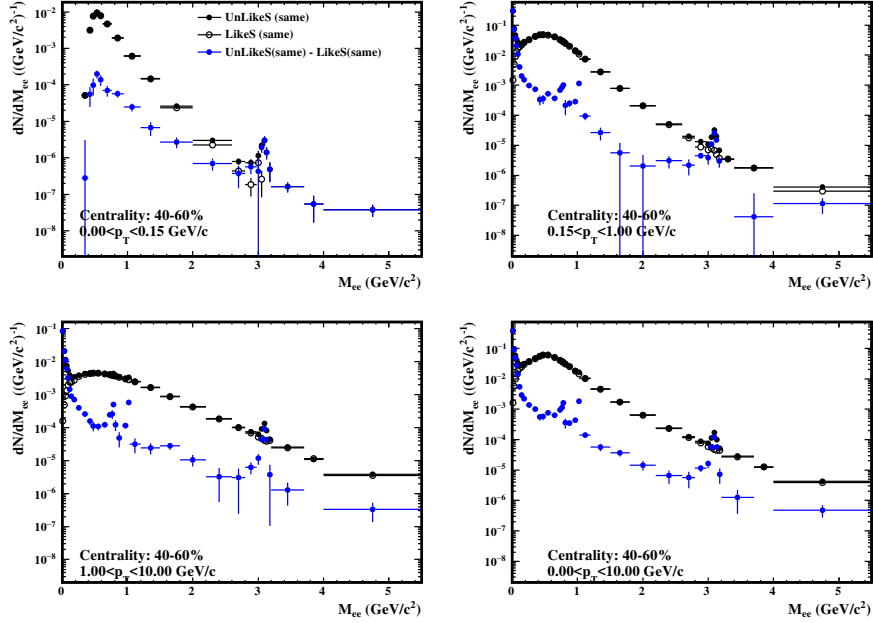


Figure 28: Run11 40-60% central Au + Au collisions at $\sqrt{s_{NN}} = 200$ GeV.

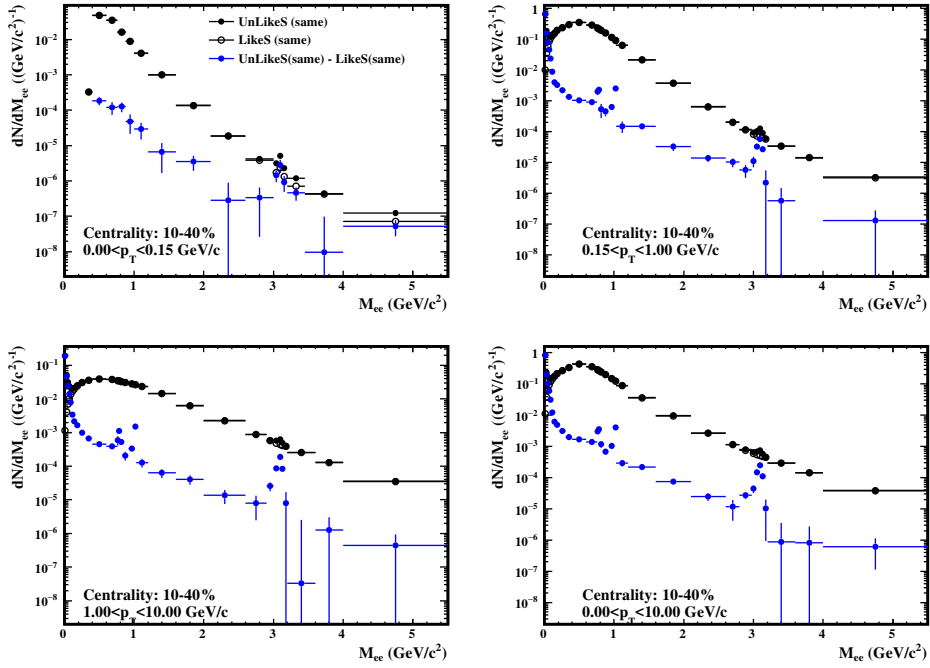


Figure 29: Run11 10-40% central Au + Au collisions at $\sqrt{s_{NN}} = 200$ GeV.

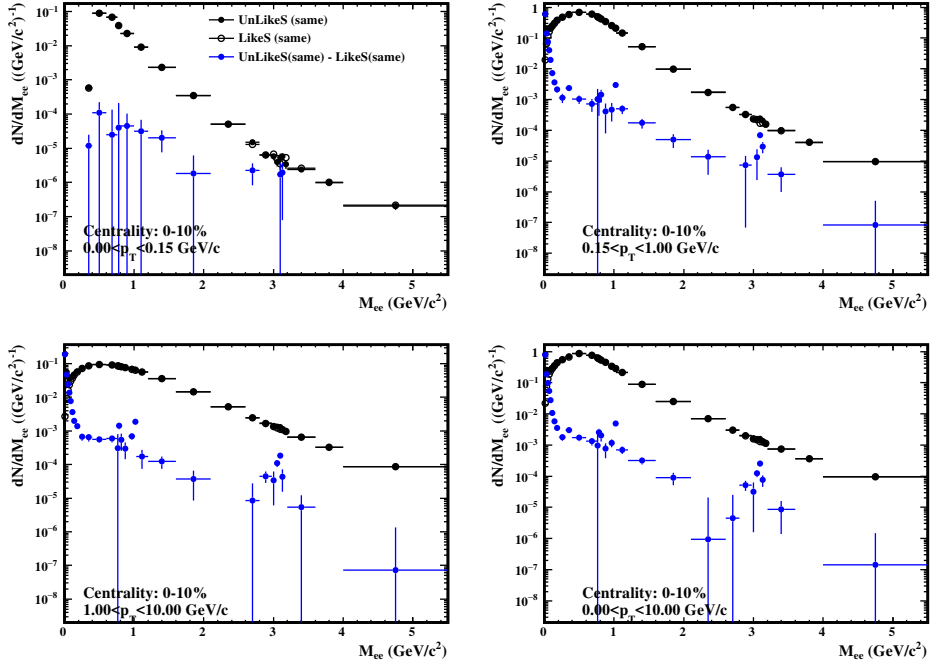


Figure 30: Run11 0-10% central Au + Au collisions at $\sqrt{s_{NN}} = 200$ GeV.

312 **4.1.1 TPC Tracking Efficiency**

313 The TPC tracking efficiency (ε_{TPC}), including the TPC response and ac-
314 ceptance, is evaluated via the standard STAR embedding technique. The
315 Monte Carlo (MC) tracks are embedded into the real data at the raw data
316 level to have a realistic detector occupancy environment. The real data is
317 randomly sampled over the entire U + U minimum-bias data set, while the
318 number of embedded MC tracks is constrained to 5% of the measured mul-
319 tiplicity of the real events to avoid a sizable impact on the realistic TPC
320 tracking efficiency. The MC tracks, with flat p_T , η , and ϕ , are generated and
321 passed through the full simulation of the STAR detector geometry using the
322 GEANT model [6], and then mixed with the real data. The mixed events
323 are processed through the exactly same off-line reconstruction chain as that
324 used in real data production. The quality assurance is made to ensure the
325 MC simulation reproduces the real data before studying the TPC tracking
326 efficiency. The TPC tracking efficiency is derived by taking the ratio of the
327 number of reconstructed MC tracks (N_{rec}), satisfying the track quality cuts
328 except nHitsDedx cut used in this analysis, over the number of embedded
329 MC tracks (N_{emb}), as shown in Eq. 7

$$\varepsilon_{TPC} = \frac{N_{rec} (nHitsFit \geq 20 \& \frac{nHitsFit}{nHitsPoss} \geq 0.52 \& dca \leq 1 \& |\eta| \leq 1)}{N_{emb} (|\eta| \leq 1)} \quad (7)$$

330 The 1-D TPC tracking efficiencies in Run12 U + U collisions at 193 GeV are
331 shown in Fig. 31. However, the 3-D (p_T , η , and ϕ) TPC tracking efficiency
332 will be used in the finally pair efficiency correction, discussed in Sec. 4.2.
333 Detailed information of 3-D TPC tracking efficiencies can be found in <https://drupal.star.bnl.gov/STAR/starnotes/private/psn0684>

335 **4.1.2 nHitsDedx Cut Efficiency**

336 The nHitsDedx cut efficiency ($\varepsilon_{nHitsDedx}$) is derived from the real data,
337 because the nHitsDedx variable from MC simulation is not consistent with

the data. The photonic electron sample (using all track quality and eID cuts except nHitsDedx and the TOF velocity cuts) is selected according to the method discussed in Sec. 2.3. The TOF velocity cut is abandoned, because it biases the nHitsDedx to a large number due to the TOF matching algorithm. The nHitsDedx cut efficiency is then derived by comparing the number of photonic electron tracks with and without nHitsDedx cut. Figure 32 shows the nHitsDedx cut efficiencies as a function of p_T in Run12 U + U collisions at 193 GeV.

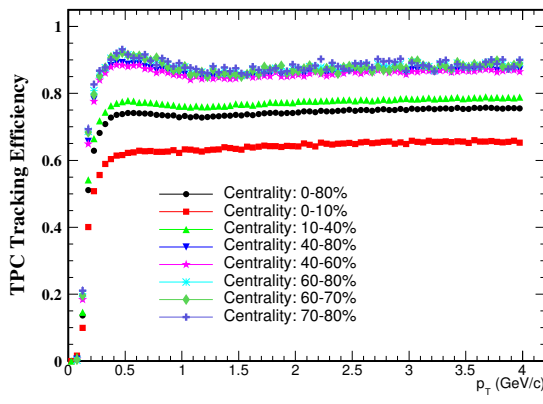


Figure 31: The 1-D TPC tracking efficiencies in Run12 U + U minimum-bias and different centrality collisions at 193 GeV.

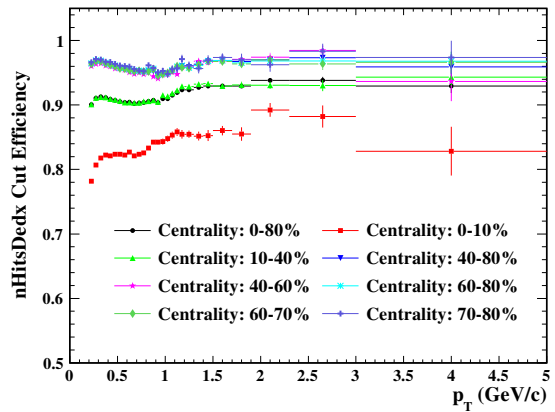


Figure 32: The nHitsDedx cut efficiency in Run12 U + U minimum-bias and different centrality collisions at 193 GeV.

4.1.3 TOF Matching Efficiency

The TOF matching efficiency (ε_{TOF}), including the TOF response and the acceptance difference between the TPC and TOF, is evaluated by the real data. It can be calculated by comparing the number of qualified primary tracks matched with the TOF (with $\beta > 0$, $N_{matched}$) over the number of qualified primary tracks (N_{TPC}). Due to the limited statistics of pure electron sample, the pure pion sample selected by a tight TPC dE/dx cut ($|n\sigma_\pi| < 0.6$), is thus used to generate the 3-D (p_T , η , and ϕ) TOF matching efficiency. The TOF matching efficiency difference between the electron and pion is

then corrected for each (η, ϕ) bin using the same p_T dependent correction factor. The TOF matching efficiency difference between electrons and pions, is due to the decay loss of pions between the TPC and TOF as well as other effects (e.g. pile-up effect). The 1-D TOF matching efficiency and the p_T dependent correction factor in Run12 U + U collisions at 193 GeV are shown in Fig. 33. 3-D TOF matching efficiencies can be find in <https://drupal.star.bnl.gov/STAR/starnotes/private/psn0684>.

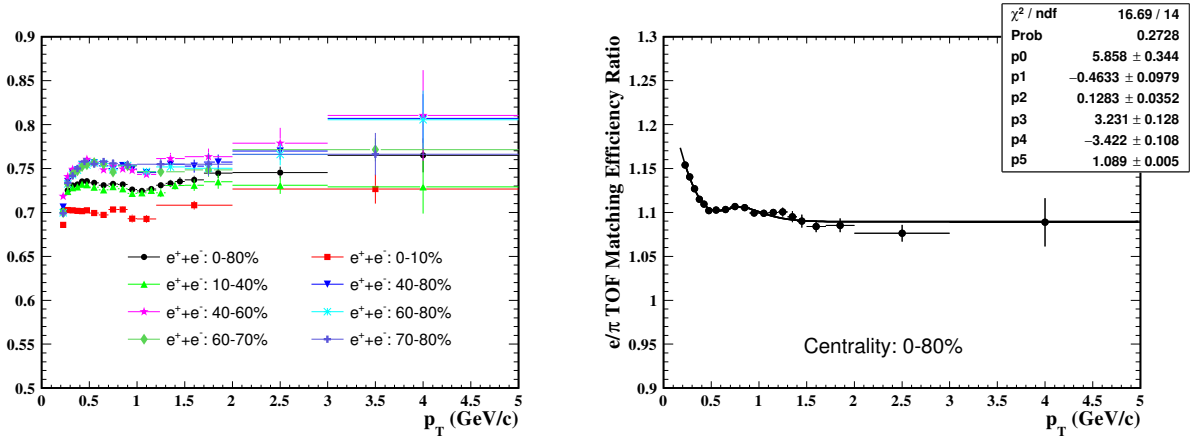


Figure 33: (Left) Centrality dependence of 1-D TOF matching efficiency for pure electron and pion sample in Run12 U + U collisions at 193 GeV. (Right) The corresponding TOF matching efficiency ratio of electron over pion as a function of p_T in Minimum-bias U + U collisions.

4.1.4 eID Cuts Efficiency

The electron identification cut efficiency (ε_{eID}) includes two components: the TOF velocity ($1/\beta$) cut efficiency and dE/dx cut ($n\sigma_e$) efficiency. Pure electron sample is used to evaluate the TOF velocity cut efficiency, and the $1/\beta$ distribution of the pure electron is shown in the left panel of Fig. 34. The red lines depict the $1/\beta$ cut used in this analysis, and the efficiency is calculated using two methods: Gaussian fitting and bin counting. The Gaussian fitting method overestimates the $1/\beta$ cut efficiency due to the tail structure in each p_T bin. Thus the default $1/\beta$ cut efficiency value, shown

in the right panel (blue circles) of Fig. 34 and Fig. 35, comes from the bin counting method, and the difference between this two methods is taken into account for the systematic uncertainty. The $n\sigma_e$ cut efficiency is derived from the multi-Gaussian fit discussed in Sec. 2.3. Figure 36 depicts the $n\sigma_e$ cut efficiency in Run12 U + U collisions at 193 GeV.

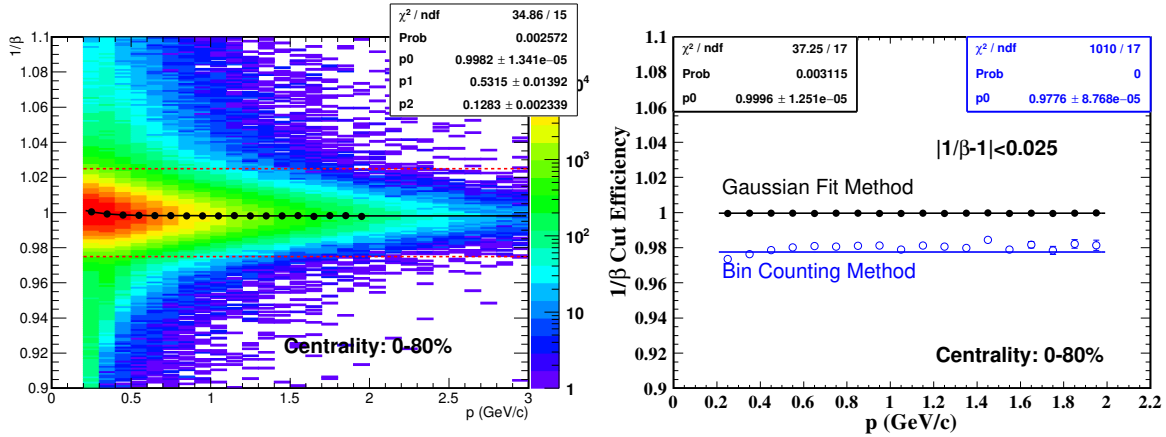


Figure 34: (Left) The $1/\beta$ distribution for pure electron sample in Run12 U + U minimum-bias collisions at 193 GeV. Red dashed lines represent the $1/\beta$ cut used in this analysis. Black dots represent the $1/\beta_{\text{mean}}$ for each p_T bin while the black curve is the fit function. (Right) The $1/\beta$ cut efficiencies using bin counting (default, blue circles) and Gaussian fit (black dots) methods.

4.2 Pair Efficiency

The dielectron pair efficiency within STAR acceptance ($p_T^e \geq 0.2$ GeV/ c , $|\eta_e| \leq 1$, $|Y_{ee}| \leq 1$) is evaluated from single track efficiency by two different simulation folding methods:

- (i) Toy MC simulation (Virtual photon simulation), which uses the virtual photon as input. The 2-D kinematics (M_{ee}, p_T) of the virtual photon is taken from the hadronic cocktail (discussed in Sec. 5) with flat rapidity (Y), azimuthal (ϕ) distribution, and the virtual photon decays into electron and positron pairs isotropically.

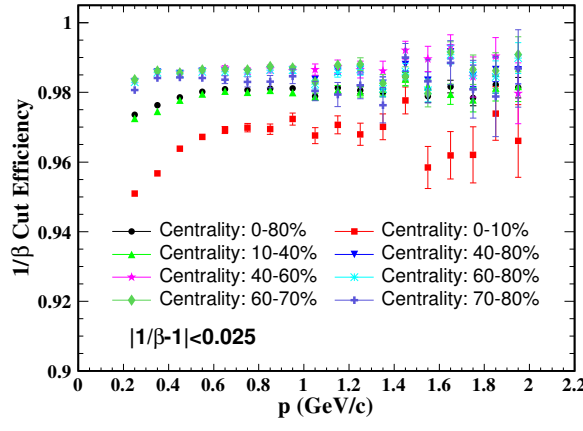


Figure 35: Centrality dependence of $1/\beta$ cut

efficiencies using bin counting method in $U + U$ collisions at 193 GeV.

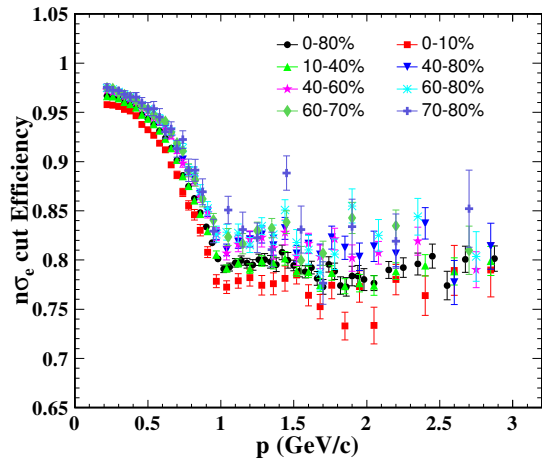


Figure 36: The $n\sigma_e$ cut efficiency in $U + U$ collisions at 193 GeV.

385 (ii) Cocktail simulation, which uses the hadronic cocktail as input, including
 386 the correlated heavy flavor decay ($c\bar{c}$, $b\bar{b}$) and Drell-Yan process from
 387 PYTHIA [7] simulation. The long-lived hadrons decay into electron and
 388 positron pairs isotropically. However, the electron and position from the
 389 heavy flavor decay are highly correlated.

390 The largest difference between these two methods is the correlated heavy
 391 flavor contribution, which is still unclear in heavy-ion collisions due to possible
 392 medium modifications of the heavy flavor correlations compared to those in
 393 $p + p$ collisions. In this analysis, the heavy flavor correlations rely on the
 394 PYTHIA simulation without any artificial modification.

395 The single track efficiencies caused by the TPC tracking and TOF match-
 396 ing are folded into pair efficiency in 3-D (p_T , η , and ϕ) momentum space while
 397 the others are folded in 1-D (p_T) momentum space. For fine centrality class,
 398 the statistics is not good enough to generate the high granularity 3-D TPC
 399 and TOF single track efficiencies. Thus, the 3-D TPC and TOF efficiencies
 400 of minimum-bias collisions are scaled to the fine centrality bin according to
 401 electron p_T dependent factor. The difference between the pair efficiencies
 402 from scaled 3-D and individual 3-D TPC&TOF efficiencies is treated as a

source of the pair efficiency systematic uncertainty. The momentum resolution and energy loss effects, discussed in Sec. 5, are also taken into account during the folding process. The pair efficiency is calculated and applied in 2-D kinematics (M_{ee}, p_T). Figure 37 shows the 2-D pair efficiency evaluated by the ‘‘Virtual Photon simulation’’ and ‘‘Cocktail simulation’’ methods in Run12 U + U minimum-bias collisions at 193 GeV. The default pair efficiency is evaluated by the ‘‘Virtual Photon simulation’’ and the difference between these two methods is taken into account for systematic uncertainty. Figure 38 shows the p_T integrated ($0 < p_T < 5 \text{ GeV}/c$) and very low p_T ($p_T < 0.15 \text{ GeV}/c$) 1-D pair efficiencies in various centrality classes. Figure 39 and Fig. 40 show the p_T integrated ($0 < p_T < 5 \text{ GeV}/c$) and very low p_T ($p_T < 0.15 \text{ GeV}/c$) 1-D pair efficiencies in various centrality classes of Run10 and Run11 Au + Au collisions at 200 GeV, separately.

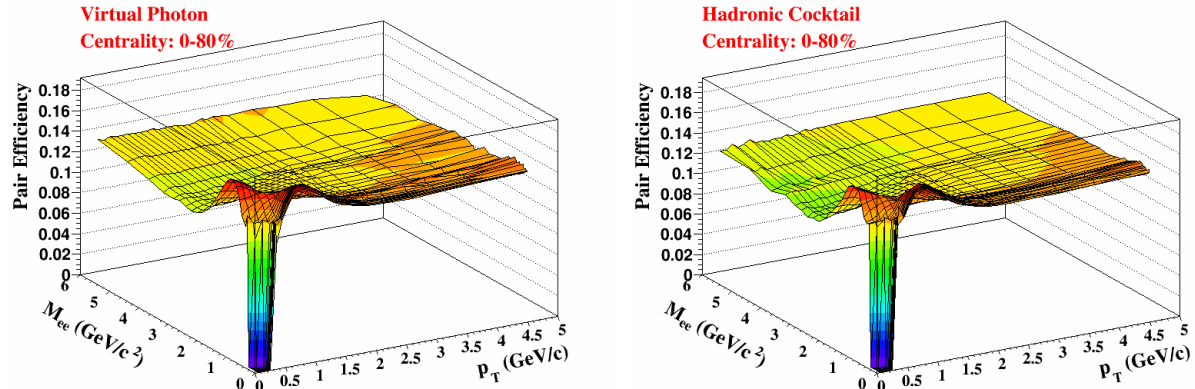


Figure 37: The 2-D pair efficiency evaluated by the ‘‘Virtual photon simulation’’ (Left) and ‘‘Cocktail simulation’’ (Right) methods in Run12 U + U minimum-bias collisions at 193 GeV.

The pair efficiencies have been also evaluated by using the $\gamma\gamma \rightarrow e^+e^-$ interaction [8] as input. In which, the pair efficiencies are compatible with that obtained from ‘Virtual Photon simulation’, demonstrating the pair efficiency within STAR acceptance ($p_T^e \geq 0.2 \text{ GeV}/c, |\eta_e| \leq 1, |Y_{ee}| \leq 1$) evaluated by folding method is not sensitive to the underlying physics mechanisms. The

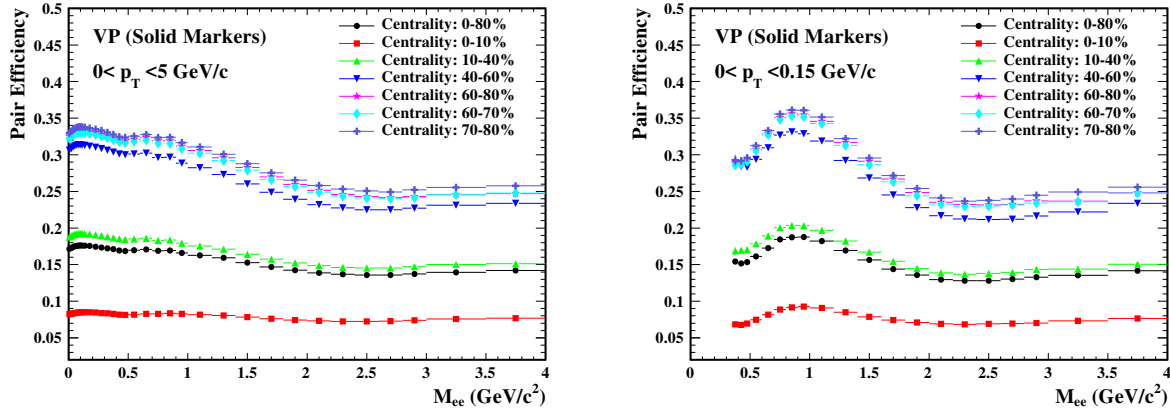


Figure 38: The p_T integrated (Left) and very low p_T (Right) 1-D pair efficiency for different centralities in Run12 U + U collisions at 193 GeV..

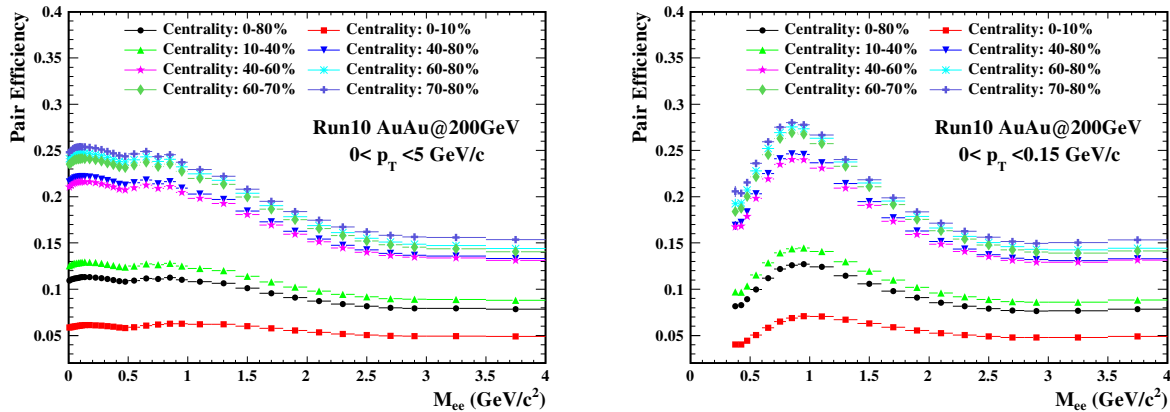


Figure 39: Centrality dependence of p_T integrated (Left) and very low p_T (Right) 1-D pair efficiency in Run10 Au + Au collisions at 200 GeV.

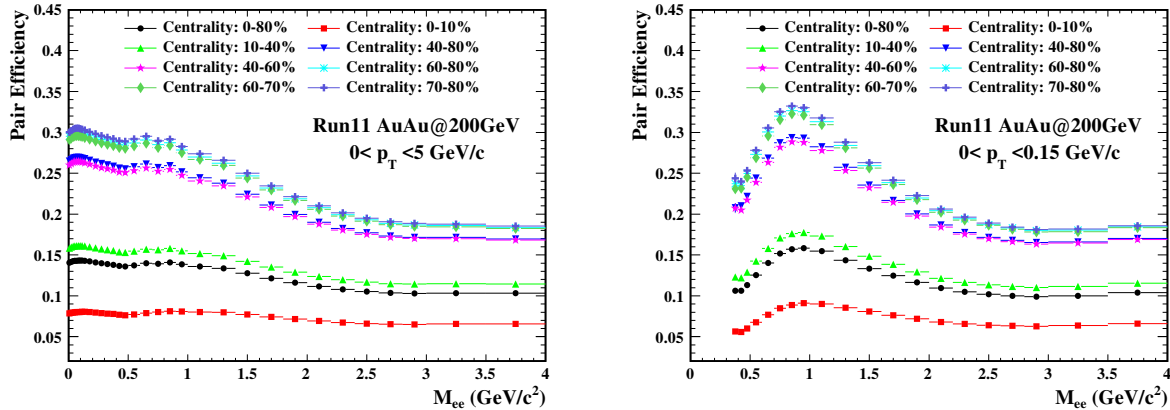


Figure 40: Centrality dependence of p_T integrated (Left) and very low p_T (Right) 1-D pair efficiency in Run11 Au + Au collisions at 200 GeV.

pair efficiency comparisons can be found in Fig. 41.

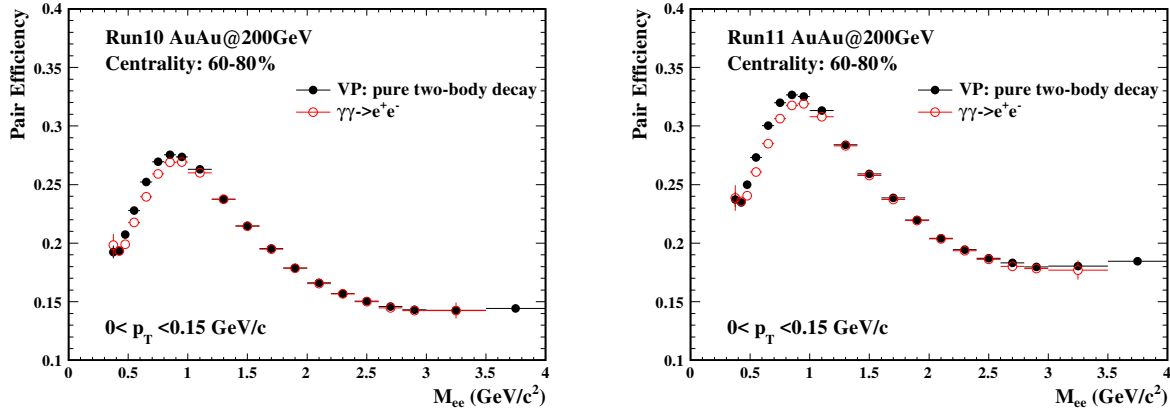


Figure 41: The comparison of pair efficiencies obtained from “Virtual photon simulation” and “ $\gamma\gamma \rightarrow e^+e^-$ simulation” methods in Run10 (Left) and Run11 (Right) Au + Au minimum-bias collisions at 200 GeV.

421

422 The ϕ_V cut (reject electron pairs) efficiency is evaluated through π^0 Dalitz
 423 decay embedding (see Sec. 4.1.1) and the virtual photon simulation. The
 424 ϕ_V cut efficiency obtained by these two methods is shown in Fig. 42. The
 425 default ϕ_V cut efficiency is evaluated by the virtual photon simulation and the
 426 difference between these two methods is taken into account for the systematic
 427 uncertainty. **The ϕ_V cut, which is only applied in $M_{ee} < 0.2$ GeV/c 2 ,**

428 has no effect at all for the very low p_T e^+e^- analysis.

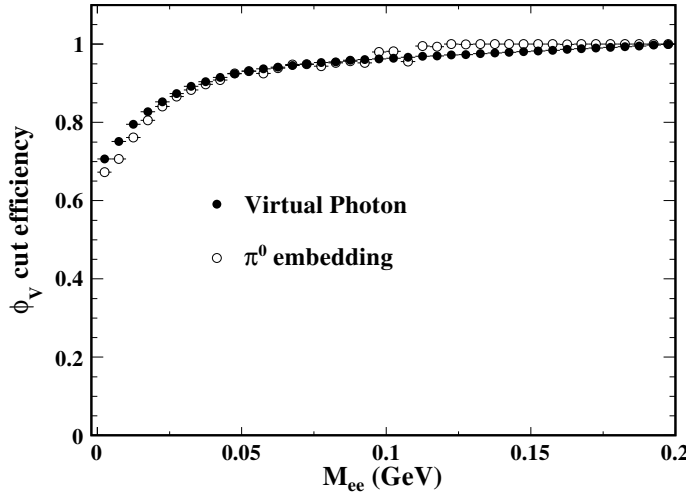


Figure 42: The ϕ_V angle cut efficiencies obtained by π^0 Dalitz decay embedding and virtual photon simulation.

429 5 Hadronic Cocktail Simulation

430 Dielectrons as measured by the detector originate from all stage in the
431 evolution of heavy-ion collisions. The contribution of the dielectron pairs from
432 hadronic decays, so called hadronic cocktail, to the final dielectron spectrum
433 can be well evaluated trough MC simulation once their yields and p_T spectra
434 are measured. The components of the cocktail simulation in this analysis are
435 listed below:

- 436 (i) Two-body decays: $\omega \rightarrow e^+e^-$, $\phi \rightarrow e^+e^-$, $J/\psi \rightarrow e^+e^-$, $\psi' \rightarrow e^+e^-$.
- 437 (ii) Dalitz decays: $\pi^0 \rightarrow \gamma e^+e^-$, $\eta \rightarrow \gamma e^+e^-$, $\eta' \rightarrow \gamma e^+e^-$, $\omega \rightarrow \pi^0 e^+e^-$,
438 $\phi \rightarrow \eta e^+e^-$.
- 439 (iii) Heavy-flavor decays: $c\bar{c} \rightarrow e^+e^- + X$, $b\bar{b} \rightarrow e^+e^- + X$.
- 440 (iv) Drell-Yan process.

⁴⁴¹ The ρ^0 , considered to be modified by the hadronic medium, is excluded in
⁴⁴² the cocktail simulation.

⁴⁴³ For U + U collisions at 193 GeV, there is no measurement for the identified
⁴⁴⁴ particle species. However, the energy density created in U + U collisions at
⁴⁴⁵ $\sqrt{s_{NN}} = 193$ GeV is only about 20% higher than that in Au + Au collisions
⁴⁴⁶ at $\sqrt{s_{NN}} = 200$ GeV [10]. Thus the hadron p_T spectra in Au + Au collisions
⁴⁴⁷ at 200 GeV [2] are employed for cocktail simulation in this analysis, as shown
⁴⁴⁸ in Fig. 43. The measurements of identified particle species (the symbols in
⁴⁴⁹ Fig. 43) except J/ψ in Au + Au collisions at 200 GeV, are simultaneously
⁴⁵⁰ fitted by a core-corona-based Tsallis Blast-Wave (TBW) model [11, 12]. The
⁴⁵¹ core and corona describe the bulk production and the hard scattering con-
⁴⁵² tributions from $p + p$ -like collisions, respectively. The J/ψ is excluded from
⁴⁵³ simultaneously fit, because the J/ψ is not considered as a component of the
⁴⁵⁴ bulk medium. The TBW fit can well describe the measured light hadron
⁴⁵⁵ spectra and also provide predictions for the meson species without measure-
⁴⁵⁶ ment (e.g. p_T spectra of all the input meson species in $p_T < 0.15$ GeV/ c)
⁴⁵⁷ using the same core TBW parameters obtained from the simultaneously fit.
⁴⁵⁸ The rapidity and azimuthal distribution of the input hadron are assumed to
⁴⁵⁹ be flat. The yields (dN/dy) of the input hadron in Au + Au collisions are
⁴⁶⁰ extracted by integrating the fits over the whole p_T region.

⁴⁶¹ The dN/dy or cross section (σ) with their uncertainties and correspond-
⁴⁶² ing decay branching ratios of various cocktail components used in Au + Au
⁴⁶³ minimum-bias collisions at 200 GeV, are summarized in [2] (TABLE III).
⁴⁶⁴ The dN/dy of cocktail hadron components (without measurements) used in
⁴⁶⁵ U + U minimum-bias collisions at 193 GeV are essentially derived from that
⁴⁶⁶ of Au + Au minimum-bias collisions at 200 GeV by N_{part} . The π^0 dN/dy
⁴⁶⁷ $((\pi^+ + \pi^-)/2)$ [13] of Au + Au collisions at 200 GeV scaled by $N_{part}/2$ as
⁴⁶⁸ a function of N_{part} , is fitted by a first-order polynomial function. The π^0
⁴⁶⁹ dN/dy of U + U collisions at 193 GeV for different centralities are eval-
⁴⁷⁰ uated by this first-order polynomial function, as shown in Fig. 44. The input

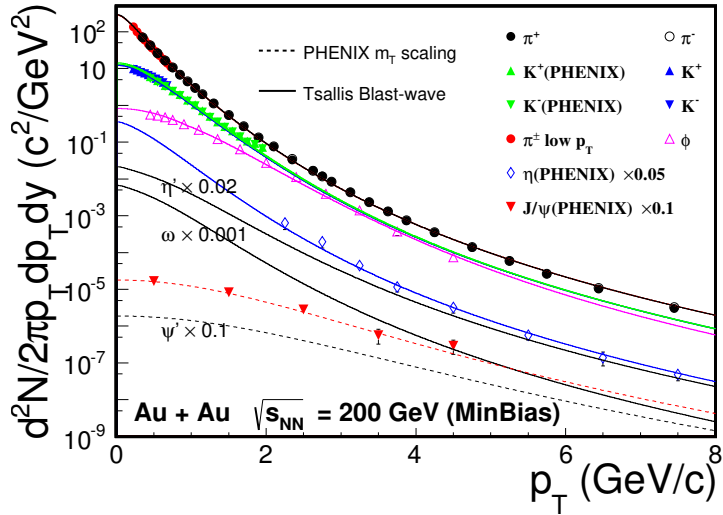


Figure 43: The invariant yields of mesons in Au + Au collisions at 200 GeV. The solid lines show the simultaneous TBW fit to the measured data points (except J/ψ) and the TBW predictions for η , η' , and ω with the same core TBW parameters. The dashed lines show the TBW fit to the measured J/ψ and the prediction for the ψ' .

⁴⁷¹ dN/dy for other cocktail hadron components (except J/ψ and ψ') in U + U
⁴⁷² minimum-bias collisions at 193 GeV are scaled with the relative pion yields,
⁴⁷³ R_{π^0} (shown in Tab. 5), with respect to Au + Au minimum-bias collisions at
⁴⁷⁴ 200 GeV. The dN/dy of J/ψ and ψ' are scaled by relative N_{coll} . The quoted
⁴⁷⁵ systematic uncertainties of the hadron yields are the same as that of Au +
⁴⁷⁶ Au collisions at 200 GeV. The input p_T spectra of cocktail hadron compo-
⁴⁷⁷ nents for different centralities in U + U collisions at 193 GeV, are also the
⁴⁷⁸ same as those (using the similar TBW function fit to the available data) of
⁴⁷⁹ the corresponding centralities in Au + Au collisions at 200 GeV. The heavy
⁴⁸⁰ flavor contributions to the hadronic cocktail will be discussed later.

⁴⁸¹ Once the kinematics (p_T , η , and ϕ) of the parent hadron obtained, the
⁴⁸² kinematics of the daughter electrons are determined by the decay kinematics.
⁴⁸³ The electron pair mass depends on the parent particle and the decay mode
⁴⁸⁴ (two-body decay or Dalitz decay). The electron pair mass of two-body decay

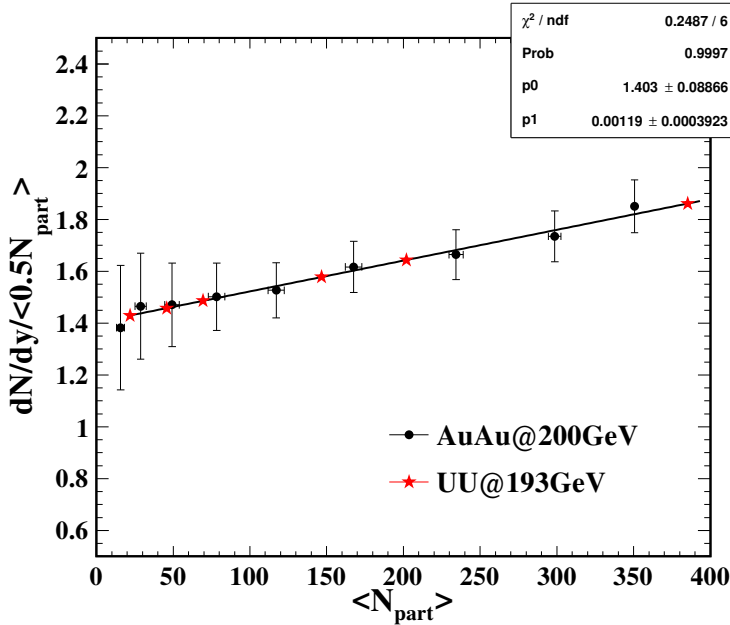


Figure 44: The π^0 yields (black dots) scaled by $N_{part}/2$ as a function of N_{part} is fitted by a first-order polynomial function (black line). The π^0 yields of U + U collisions for different centralities (red stars) are evaluated by this fit function.

Table 5: The scale factors (R_{π^0}) for different centralities in U + U collisions at 193 GeV, with respect to the dN_{π^0}/dy (98.49) Au + Au minimum-bias collisions at 200 GeV.

Centrality (%)	dN_{π^0}/dy	R_{π^0}	$\langle N_{coll} \rangle$
0-80	115.76	1.175	350.08
60-80	15.72	0.160	22.48
40-80	33.35	0.339	63.05
40-60	51.65	0.524	103.61
10-40	165.90	1.684	467.44
0-10	358.48	3.640	1146.12

⁴⁸⁵ follows a narrow Breit-Wigner distribution as given in Eq. 8

$$\frac{dN}{dM_{ee}} = \frac{2\Gamma_0}{(M_{ee} - M_h)^2 + \Gamma_0^2/4} \quad (8)$$

⁴⁸⁶ where the Γ_0 represents the PDG [14] width, and M_h is the mass of the hadron
⁴⁸⁷ which decays into the dielectron. The electron pair mass (M_{ee}) is constrained
⁴⁸⁸ to $[2m_e, 4 \text{ GeV}/c^2]$, where the m_e is the electron mass. The electron pair mass
⁴⁸⁹ of Dalitz decay follows the Kroll-Wada formula [15] as given in Eq. 9,

$$\frac{dN}{dM_{ee}} = PS \cdot |F(M_{ee}^2)|^2 \cdot QED \quad (9)$$

⁴⁹⁰ Where PS is the phase space term defined in Eq. 10. The M_h is mass of the
⁴⁹¹ hadron which undergoes a Dalitz decay process ($h \rightarrow X e^+ e^-$) and X is the
⁴⁹² third daughter particle with a mass M_X . if X is massless (e.g. γ in π^0, η, η'
⁴⁹³ Dalitz decay), the phase space term simplifies to Eq. 11.

$$PS = \left(\left(1 + \frac{M_{ee}^2}{M_h^2 - M_X^2} \right)^2 - \frac{4M_h^2 M_{ee}^2}{(M_h^2 - M_X^2)^2} \right)^{\frac{3}{2}} \quad (10)$$

⁴⁹⁴

$$PS = \left(1 - \frac{M_{ee}^2}{M_h^2} \right)^3 \quad (11)$$

⁴⁹⁵ The QED term is described by Eq. 12, where N represents a degeneracy
⁴⁹⁶ factor that depends on how many photons can convert. N is 4 for ω and ϕ
⁴⁹⁷ while it is 2 for other hadrons undergoing Dalitz decay process, involved in
⁴⁹⁸ this analysis. The α is the fine-structure constant ($\sim 1/137$).

$$QED = \frac{N \cdot \alpha}{3\pi} \sqrt{1 - \frac{4m_e^2}{M_{ee}^2}} \left(1 + \frac{2m_e^2}{M_{ee}^2} \right) \frac{1}{M_{ee}} \quad (12)$$

⁴⁹⁹ The $|F(M_{ee}^2)|^2$ is the electromagnetic form factor. The form factor, described
⁵⁰⁰ in Eq. 13, is used for almost all Dalitz decay involved in this analysis except
⁵⁰¹ η' .

$$|F(M_{ee}^2)|^2 = \left(\frac{1}{1 - M_{ee}^2 \Lambda^{-2}} \right)^2 \quad (13)$$

where the Λ^{-2} is the form factor slope, listed in Tab. 6. For π^0 the form factor is usually given by Eq. 14,

$$|F(M_{ee}^2)|^2 = (1 + M_{ee}^2 \Lambda^{-2})^2 \quad (14)$$

For η' , the form factor is given by Eq. 15. The Λ^{-2} and Γ_0^2 are from the fit to the data presented in [18], where the Λ^{-2} and Γ_0^2 are 1.8396 and 1.99×10^{-2} , respectively.

$$|F(M_{ee}^2)|^2 = \frac{1}{(1 - M_{ee}^2 \Lambda^{-2})^2 + \Gamma_0^2 \Lambda^{-2}} \quad (15)$$

Table 6: The electromagnetic form factor slope of mesons.

Meson	Λ^{-2}
π^0	1.756 [16]
η	1.95 [17]
η'	1.8396 [18]
ω	2.24 [17]
ϕ	3.8 [19]

The correlated heavy flavor contributions ($c\bar{c}$, $b\bar{b}$, and Drell-Yan) to the cocktail are obtained from the PYTHIA [7] simulation. These three sources are first simulated in $p + p$ collisions and then scaled by N_{coll} , listed in Tab. 5, to account for the contributions in U + U collisions. The parameter settings (other parameters use the default PYTHIA tune) for different heavy flavors in PYTHIA (version 6.419) are listed below:

- (i) $c\bar{c}$: MSEL = 1 (minimum-bias trigger), PARP(91) = 1 ($\langle k_T \rangle = 1.0$ GeV/c), PARP(67) = 1.0 (parton shower level).
- (ii) $b\bar{b}$: MSEL = 5 (b trigger), PARP(91) = 1.5 ($\langle k_T \rangle = 1.5$ GeV/c).
- (iii) Drell-Yan: MSEL = 11 (Z_0 or γ^* trigger), PARP(91) = 1.5 ($\langle k_T \rangle = 1.5$ GeV/c).

518 The charm settings are tuned to match the STAR measurement of the charmed-
 519 meson spectrum in $p + p$ collisions [20]. The input charm-pair production
 520 cross section is also from the STAR measurements [20, 21]. The Drell-Yan
 521 setting are tuned to match the theoretical calculation, and the same PYTHIA
 522 settings (except trigger setting) are used in the bottom simulation. The input
 523 bottom and Drell-Yan production cross sections are $\sigma_{pp}^{b\bar{b}} = 37 \mu\text{b}$, $\sigma_{pp}^{DY} = 42$
 524 nb.

525 All the physics results reported in Chap. 7 are not corrected for the STAR
 526 detector resolution. It's very challenging to precisely reproduce the momen-
 527 tum resolution through embedding, due to various distortion effects in the
 528 TPC in the high luminosity RHIC environment. However, a data-driven
 529 method is involved in the hadronic cocktail simulation, accounting for these
 530 effects [2]. In the Run12 U + U minimum-bias embedding, the reconstructed
 531 electron p_T^{rec} probability at a given input p_T^{MC} can be described by a double
 532 crystal ball function, given in Eq. 16

$$P(p_T^{rec}, p_T^{MC}) \propto \begin{cases} A \times (B - R)^{-n}, & R < -\alpha \\ e^{-\frac{R^2}{2}}, & -\alpha \leq R < \beta \\ C \times (D + R)^{-m}, & R \geq \beta \end{cases} \quad (16)$$

533 with

$$\begin{aligned} A &= \left(\frac{n}{|\alpha|} \right)^n \times e^{-\frac{\alpha^2}{2}} \\ B &= \frac{n}{|\alpha|} - |\alpha| \\ C &= \left(\frac{m}{|\beta|} \right)^m \times e^{-\frac{\beta^2}{2}} \\ D &= \frac{m}{|\beta|} - |\beta| \\ R &= \left(\frac{p_T^{rec} - p_T^{MC}}{p_T^{MC}} - \mu \right) / \frac{\sigma_{p_T}}{p_T} \end{aligned} \quad (17)$$

534 where $n = 1.29$, $\alpha = 1.75$, $m = 2.92$, and $\beta = 1.84$ in Run10 and Run11 Au
 535 + Au minimum-bias collisions at 200 GeV [2], are employed in this analysis.

536 The $\mu = -0.001$ is slightly shifted from 0, because the energy loss is taken
 537 into account for STAR tracking with an assumption that all tracks are pions.

538 The electron p_T resolution (σ_{p_T}/p_T) as a function of p_T is evaluated from
 539 Run12 U + U embedding, shown in Fig. 45. This distribution can be de-
 540 scribed by Eq. 18,

$$\sigma_{p_T}/p_T = \sqrt{(a \times p_T)^2 + b^2} \quad (18)$$

541 The two parameters of Eq. 18 are tuned to match the J/ψ signal from the
 542 simulation with that from data. These two parameters used in this analysis
 543 are also the same as that used in Run10 and Run11 minimum-bias collisions
 544 at 200 GeV [2], which are $a = 6.0 \times 10^{-3}$ c/GeV and $b = 8.3 \times 10^{-3}$.

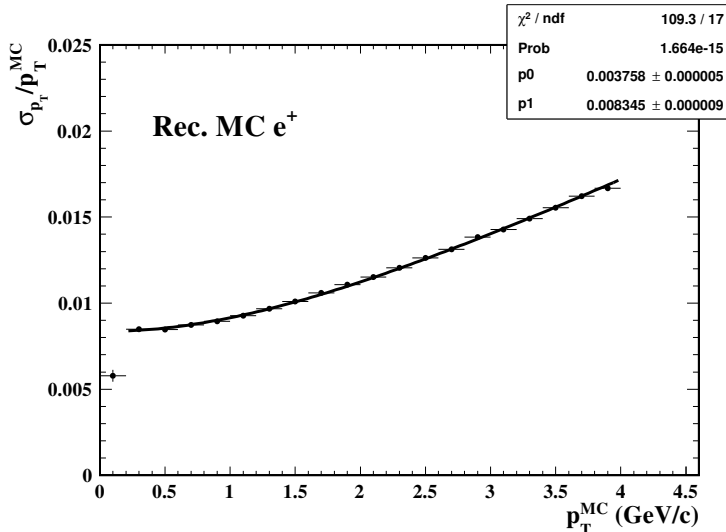


Figure 45: The transverse momentum resolution for positron as a function of p_T from Run12 U + U minimum-bias embedding sample.

545 Figure 46 shows the cocktail simulation within STAR acceptance including
 546 the light hadrons decay and correlated heavy flavor decay in U + U minimum-
 547 bias collisions at 193 GeV. The cocktails of different acceptance settings and
 548 the cocktail within STAR acceptance including the detector efficiency losses
 549 in U + U minimum-bias collisions at 193 GeV are depicted in Fig. 47. As
 550 discussed in Sec. 4.2, the dielectron pair efficiency within STAR acceptance
 551 and STAR acceptance factor can be evaluated from Fig. 47.

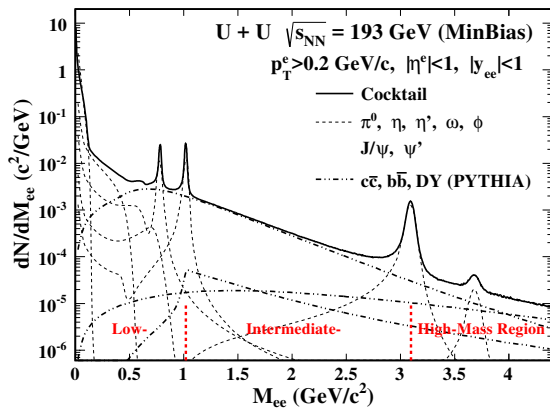


Figure 46: The cocktail simulation within STAR acceptance (solid line) including the light hadrons decay and correlated heavy flavor decay (dashed lines) in $U + U$ minimum-bias collisions at 193 GeV.

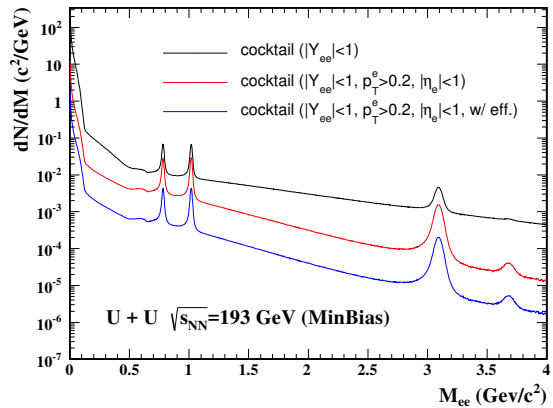


Figure 47: The cocktails of different acceptance settings (Black - before filtering STAR acceptance; Red - within STAR acceptance) and the cocktail within STAR acceptance including the detector efficiency losses (Blue) in $U + U$ minimum-bias collisions at 193 GeV.

552 6 Systematic Uncertainties

553 The sources of the systematic uncertainty that contribute to the final result
 554 in this analysis are listed below:

- 555 (i) Background subtraction.
- 556 (ii) Hadron contamination.
- 557 (iii) Efficiency correction.
- 558 (iv) Cocktail simulation.

559 **Background subtraction** In this analysis, the acceptance corrected like-sign
 560 background is subtracted for obtaining the raw signal. Where the acceptance
 561 factor is calculated by the ratio of the mixed-event unlike-sign and like-
 562 sign distribution. The systematic uncertainty of the acceptance factor can be
 563 evaluated by varying the event categories (varying the number of V_z , central-
 564 ity and event-plane bins) and event-pool size. The difference between 2-D

565 (M_{ee} , p_T^{ee}) and 1-D (M_{ee}) acceptance corrections is also taken into account
566 only for the regular dielectron analysis. For this very low $p_T e^+e^-$ analysis
567 in Au + Au and U + U collisions, the unlike-sign and like-sign acceptance
568 difference correction factor results in 1-8% p_T , mass dependent uncertainty.

569 **Hadron contamination** The identified electron candidates contain a small
570 amount of fast hadrons, as discussed in Sec. 2.3. If these hadrons are cor-
571 related with other particles (e.g. resonance decays), they may contribute
572 into the final signal spectrum. The electron purity and the relative ratios of
573 hadron over electron in the identified electron sample are shown in Fig. 9 and
574 Fig. 48, respectively. To estimate the contribution of the hadron contamina-
575 tion, the pure hadron samples are firstly selected by a tight m^2 cut (shown in
576 Fig. 3). We randomly picked hadrons from these pure samples according to
577 the hadron contamination levels in both total and the p_T differential yields,
578 creating a hadron pool. The same procedure used in the dielectron analysis
579 is applied to the hadron contamination pool to estimate the $e - h$ and $h - h$
580 contribution. The effect in U + U collisions at 193 GeV is similar to that in
581 Au + Au collisions at 200 GeV. According to the published STAR dielectron
582 long paper [2], the relative contribution to the final spectrum at very low p_T
583 is <4%.

584 **Efficiency correction** The systematic uncertainty caused by efficiency correc-
585 tion includes uncertainties on the single track efficiency which is folded into
586 the pair efficiency, the pair efficiency evaluated by different methods and the
587 ϕ_V cut efficiency. The systematic uncertainty on TPC tracking efficiency
588 (nHitsFit, dca) is evaluated by varying the selection cuts in the data and MC
589 embedding at the same time and then comparing the difference between the
590 change of data and MC embedding. The systematic uncertainties on nHits-
591 Dedx cut, $n\sigma_e$ cut and the TOF matching are evaluated by comparing the
592 corresponding efficiency differences between different pure electron samples

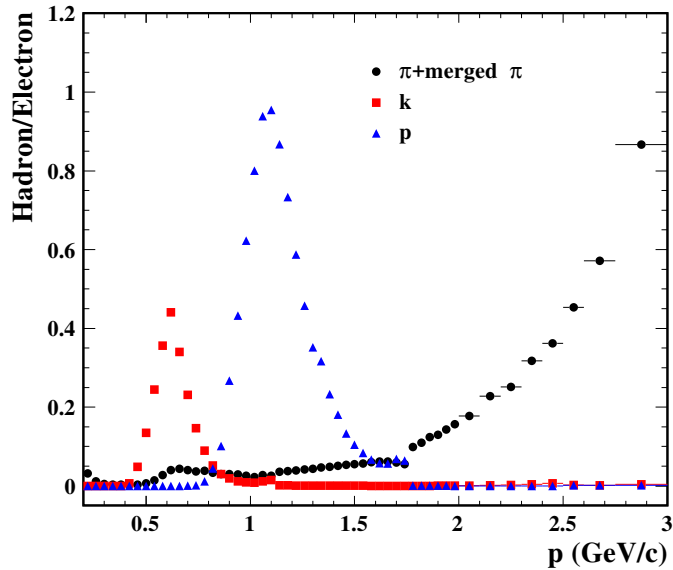


Figure 48: The relative ratio of hadrons over electrons in the identified electron sample as a function of momentum in $U + U$ minimum-bias collisions at 193 GeV.

(using different invariant mass cuts to select the pure electron samples). The systematic uncertainty on the $1/\beta$ cut efficiency is evaluated by comparing the efficiency difference between direct bin counting method and Gaussian fit (discussed in Sec. 4.1.4). These systematic uncertainties owing to the single track efficiency are summarized in Tab. 7. Due to the unknown heavy flavor correlation in the medium, two extreme methods (discussed in Sec. 4.2) are employed to fold the single track efficiency into the pair efficiency. The difference of the pair efficiency between these two methods are also taken into account for the efficiency correction systematic uncertainty. Moreover, the difference between the pair efficiencies from scaled 3-D and individual 3-D TPC&TOF efficiencies is treated as another source of efficiency correction systematic uncertainty. Combining all the aforementioned components, the uncertainties on the detector efficiency correction are $\sim 13\text{-}20\%$ (see details in p19-p20 of Ref. [2]) and $\sim 10\text{-}18\%$ in $Au + Au$ and $U + U$ collisions, respectively. The systematic uncertainty of the ϕ_V cut efficiency, only considered in regular dielectron analysis, is evaluated by comparing the difference between

the efficiency from the π^0 embedding sample and the virtual photon decay sample.

Cocktail simulation The systematic uncertainty of the cocktail simulation is evaluated by folding the systematic uncertainties of meson yields and the heavy flavor cross sections.

The total systematic uncertainty is determined via the quadratic sum of the contribution of each component. The overall uncertainties as a function of M_{ee} , p_T^{ee} for U + U and Au + Au collisions can be found in Figs. 49, 50, 51, and 52, respectively.

Table 7: Systematic uncertainties on single track efficiency.

	Component	Uncertainty (%)
TPC	nHitsFit	3.4
	DCA	1.8
	nHitsdEdx	1.1
TOF	$n\sigma_e$	0.5
	Matching	1.4
	$1/\beta$	2.4
	Total	4.9

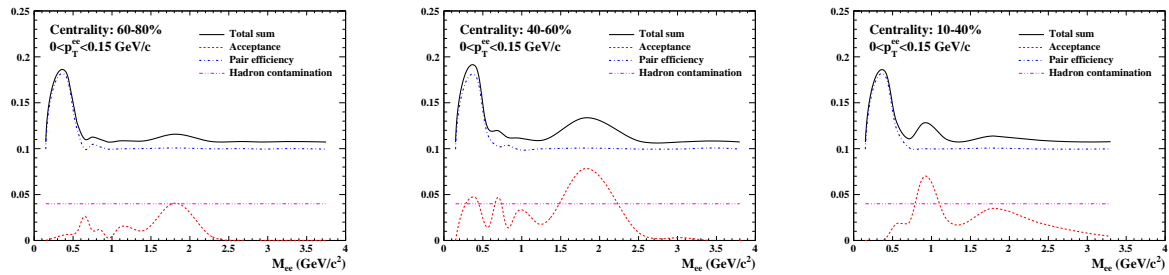


Figure 49: The overall systematic uncertainties as a function of M_{ee} for $p_T^{ee} < 0.15 \text{ GeV}/c$ in 60-80%, 40-60%, and 10-40% U + U collisions.

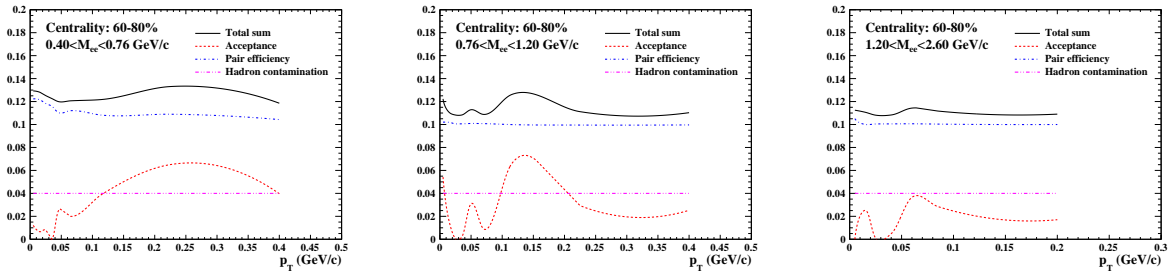


Figure 50: The overall systematic uncertainties as a function of p_T^{ee} for three different mass regions in 60-80% U + U collisions.

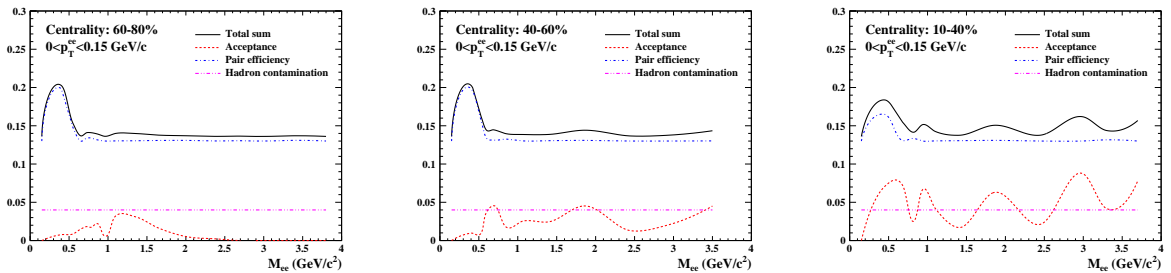


Figure 51: The overall systematic uncertainties as a function of M_{ee} for $p_T^{ee} < 0.15 \text{ GeV}/c$ in 60-80%, 40-60%, and 10-40% Au + Au collisions.

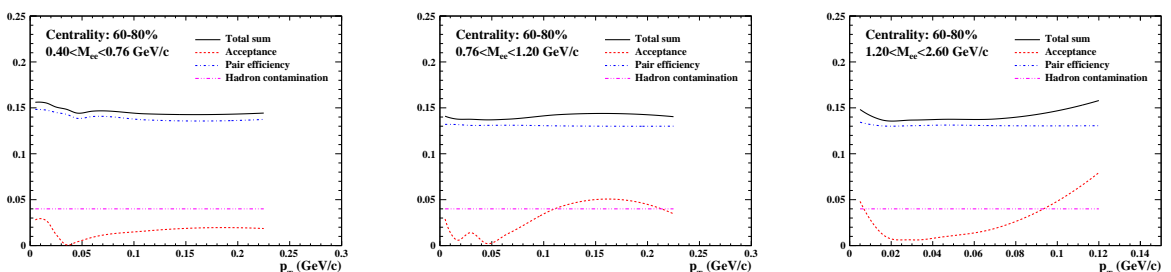


Figure 52: The overall systematic uncertainties as a function of p_T^{ee} for three different mass regions in 60-80% Au + Au collisions.

618 7 Physics Results

619 7.1 Consistency Check Between Run10 and Run11 Au + Au Col- 620 lisions

621 For the Au + Au minimum-bias triggered data, the efficiency corrected
 622 spectra are obtained separately for run 2010 and run 2011, and then combined
 623 point by point according to their relative statistical uncertainties. Before
 624 combining the results, consistency check between these two runs has been
 625 done, which are shown in Fig. 53, 54, 55, 56, and 57.

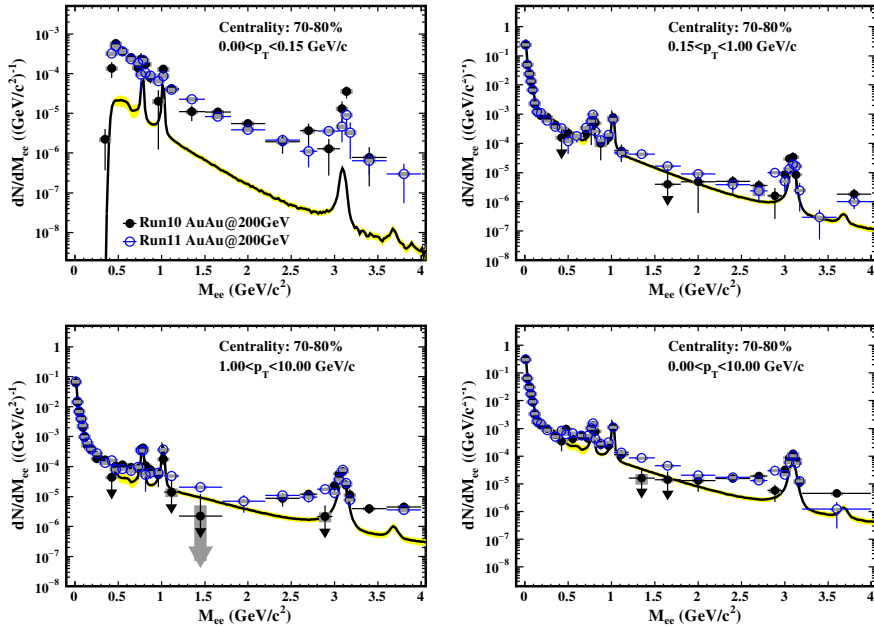


Figure 53: The efficiency-corrected mass spectra within STAR acceptance from 70-80% central Run10 and Run11 Au + Au collisions in various p_T bins.

626 7.2 Low p_T e^+e^- Paper Plots

627 To measure the true other than fiducial excess yields, the detector accep-
 628 tance effect ($p_T^e \geq 0.2 \text{ GeV}/c, |\eta_e| \leq 1, |Y_{ee}| \leq 1$) should be corrected for. The
 629 acceptance factor is estimated as the yield ratio of reconstructed e^+e^- pairs

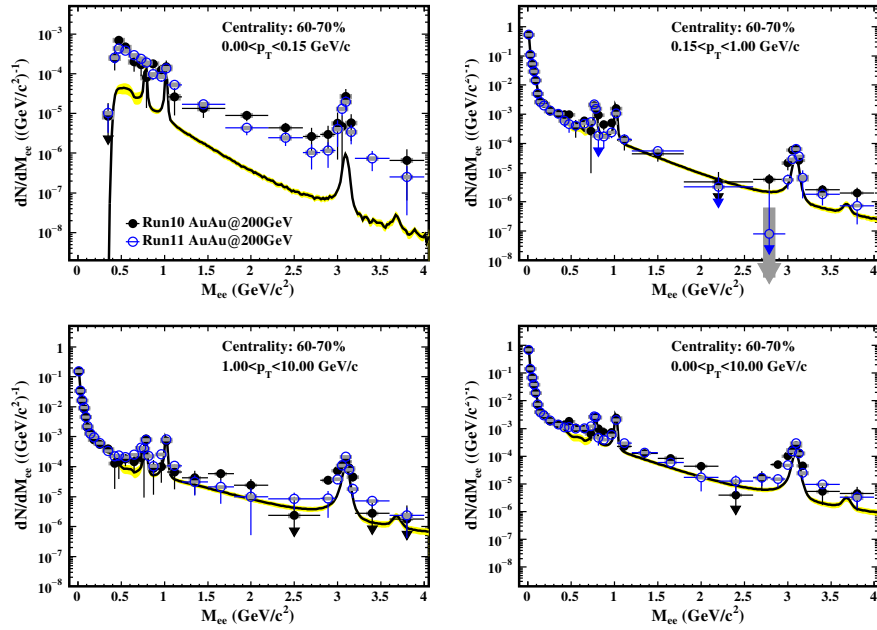


Figure 54: The efficiency-corrected mass spectra within STAR acceptance from 60-70% central Run10 and Run11 Au + Au collisions in various p_T bins.

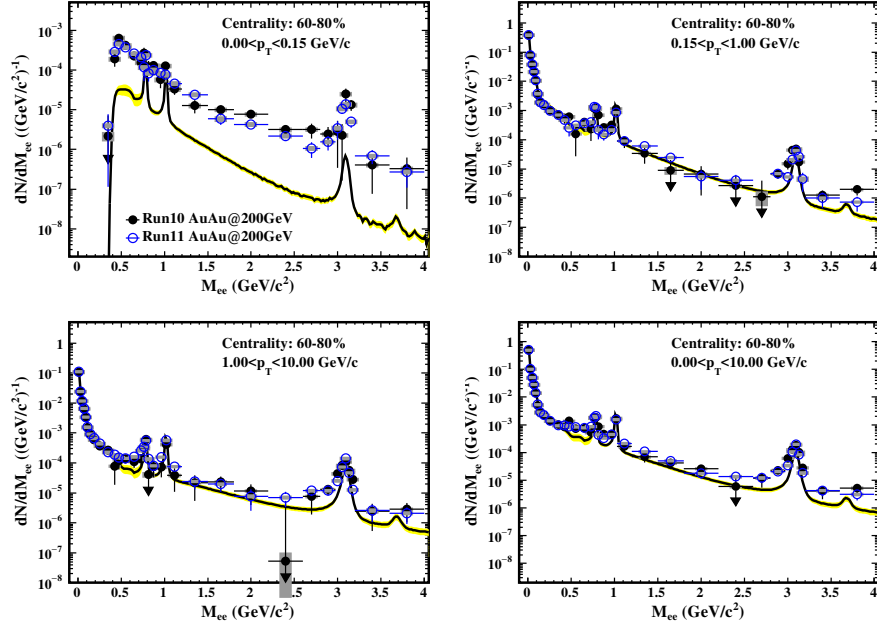


Figure 55: The efficiency-corrected mass spectra within STAR acceptance from 60-80% central Run10 and Run11 Au + Au collisions in various p_T bins.

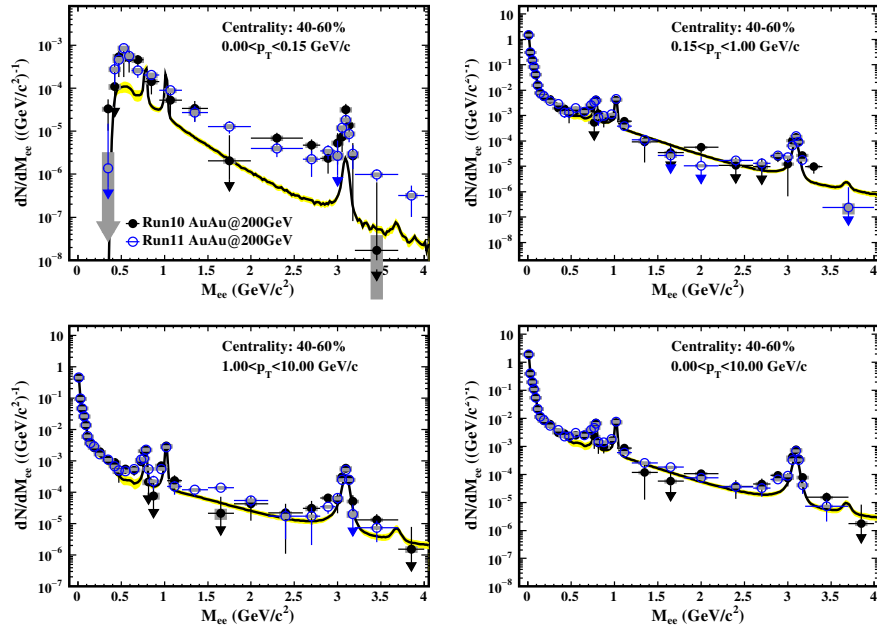


Figure 56: The efficiency-corrected mass spectra within STAR acceptance from 40-60% central Run10 and Run11 Au + Au collisions in various p_T bins.

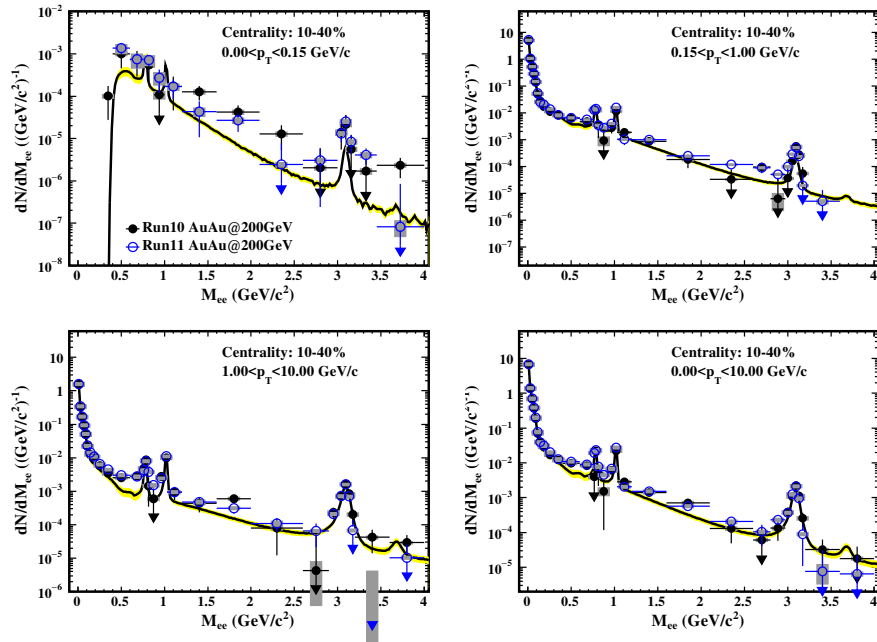


Figure 57: The efficiency-corrected mass spectra within STAR acceptance from 10-40% central Run10 and Run11 Au + Au collisions in various p_T bins.

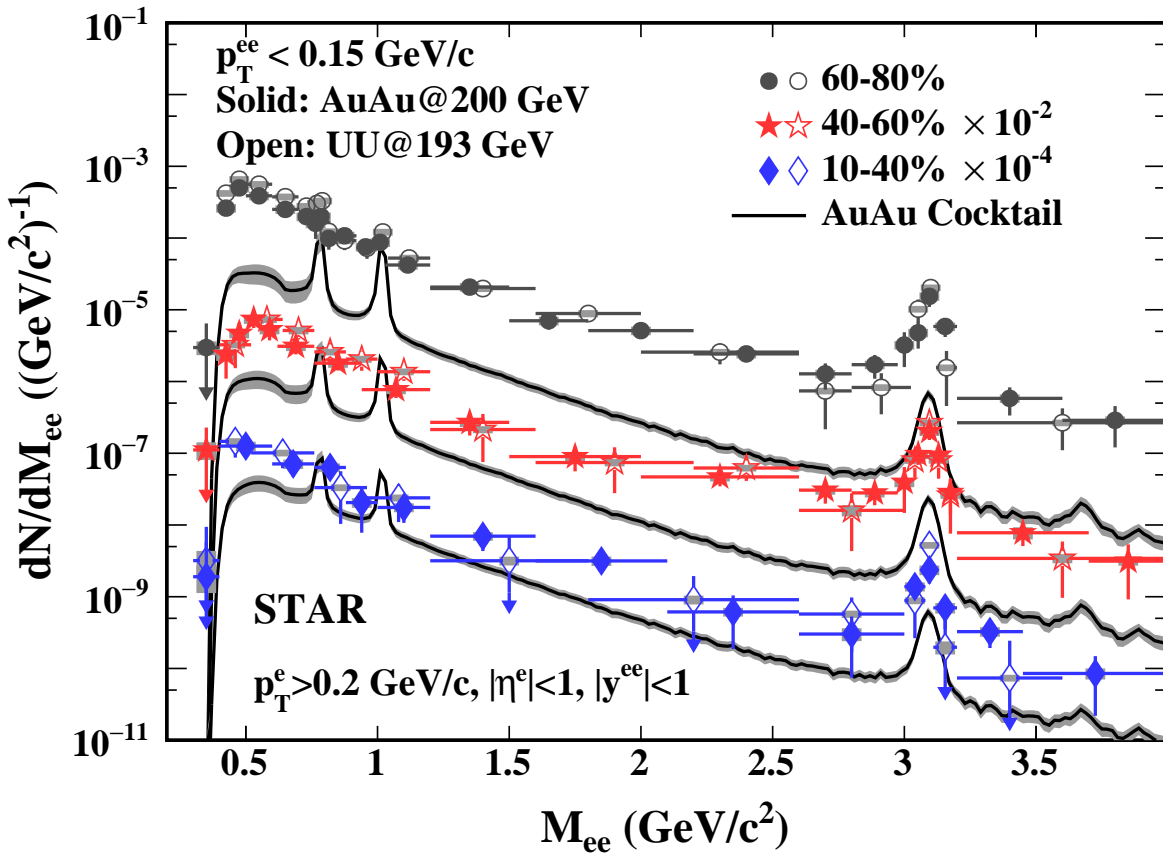


Figure 58: Centrality dependence of e^+e^- invariant mass spectrum within the STAR acceptance ($p_T^e > 0.2 \text{ GeV}/c$, $|\eta^e| < 1$, and $|y^{ee}| < 1$) from Au + Au collisions (solid markers) and U + U collisions (open markers) for $p_T < 0.15 \text{ GeV}/c$. The vertical bars on data points depict the statistical uncertainties and the horizontal bars indicate the bin width, while the systematic uncertainties are shown as grey boxes. The hadronic cocktails from U + U collisions are only $\sim 5\text{-}12\%$ higher than those from Au + Au collisions in given centrality bins. The mass spectra are compared to hadronic cocktail simulations shown here only for Au+Au collisions as solid lines with shaded bands representing the systematic uncertainty in the cocktail.

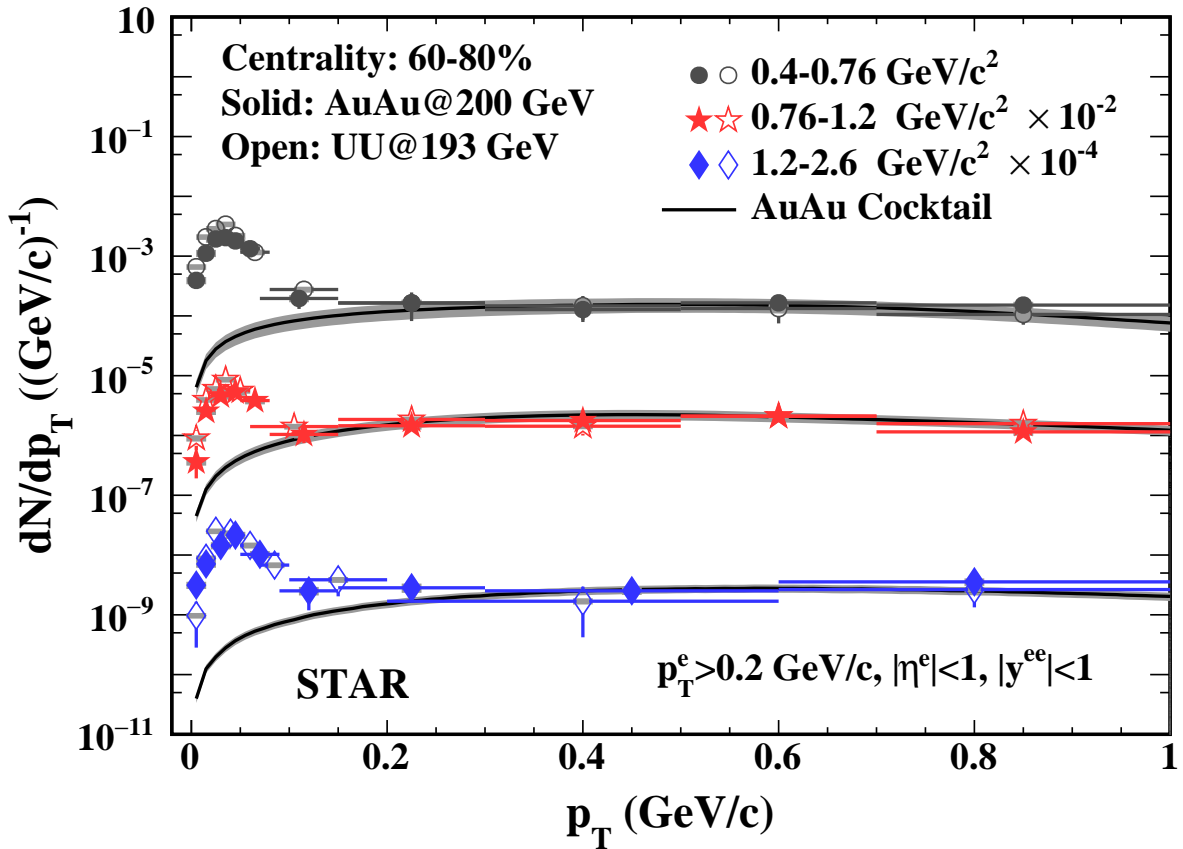


Figure 59: The e^+e^- pair p_T distributions within STAR acceptance for different mass regions in 60-80% Au+Au (solid markers) and U+U (open markers) collisions compared to cocktail simulations (solid curves). The systematic uncertainties of the data are shown as gray boxes. The brown bands depict the systematic uncertainties of the cocktail simulations.

Table 8: The χ^2/NDF values of all the fittings in Fig. 61. The “w/o” stands for without STAR acceptance corrected for while “w/” stands for with STAR acceptance corrected for.

Mass (GeV/c^2)	Au + Au w/o (w/)	U + U w/o (w/)
0.4-0.76	2.46/4 (1.47/4)	0.92/2 (1.16/2)
0.76-1.2	0.99/3 (1.10/3)	0.79/2 (0.82/2)
1.2-2.6	0.31/2 (0.55/2)	0.34/3 (0.45/3)

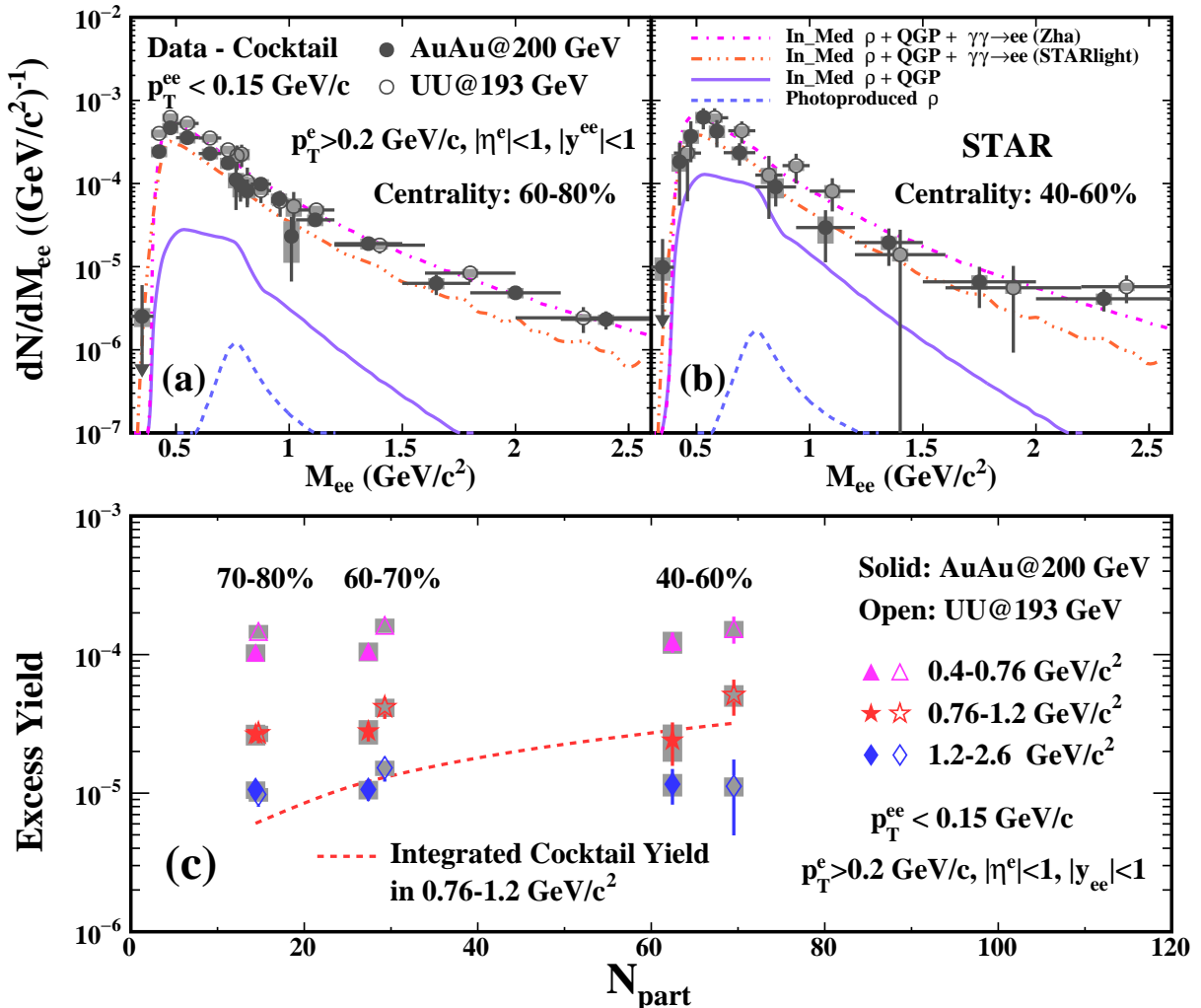


Figure 60: The low p_T ($p_T < 0.15 \text{ GeV}/c$) e^+e^- excess mass spectra (data-cocktail) within STAR acceptance in 60-80% (a), 40-60% (b) for Au+Au (solid dots) and U+U (open circles) collisions, compared with a broadened ρ model calculation (solid line). The contribution of ρ from the photonuclear process is shown, as are the contributions of photon-photon process from two models [8, 9]. Panel (c) shows the centrality dependence of integrated excess yields in the mass regions of 0.4-0.76, 0.76-1.2, and 1.2-2.6 GeV/c^2 in Au + Au (solid markers) and U + U (open markers) collisions. The centrality dependence of hadronic cocktail yields in the mass region of 0.76-1.2 GeV/c^2 is also shown for comparison. The systematic uncertainties of the data are shown as gray boxes.

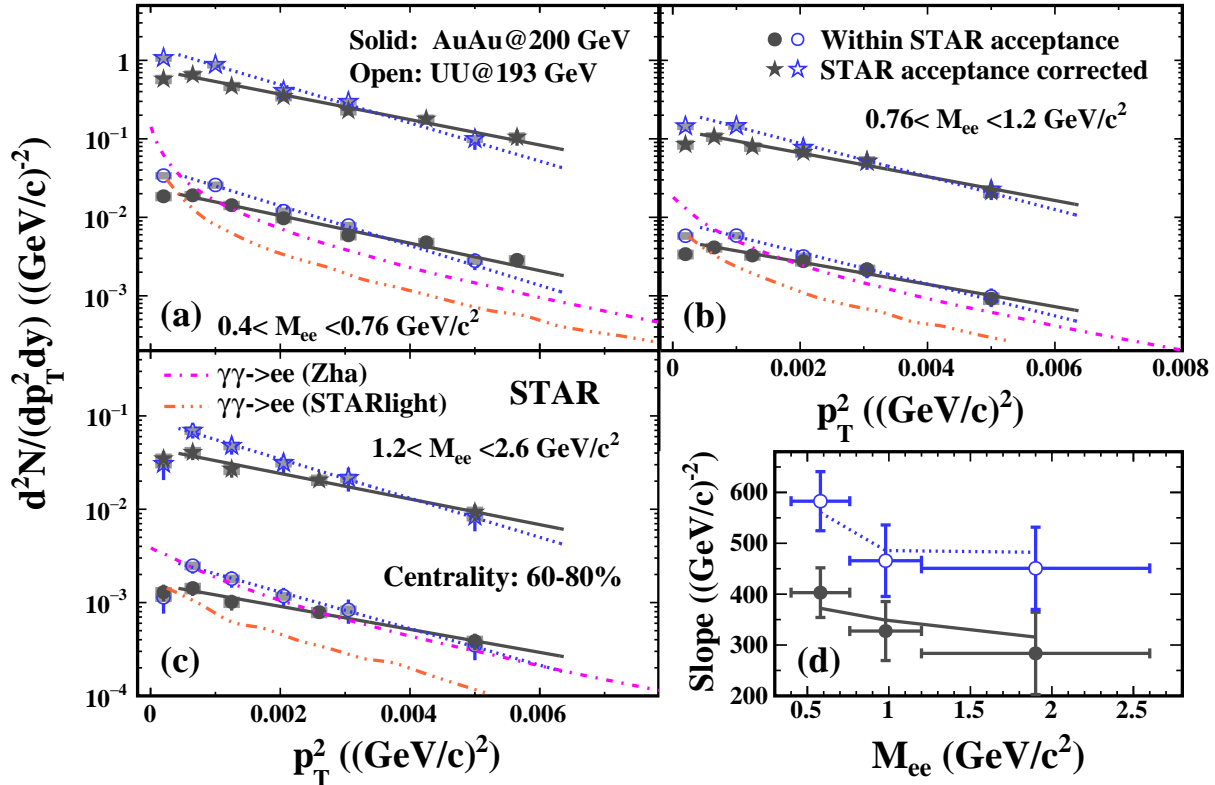


Figure 61: The p_T^2 distributions of excess yields within (solid and open circles) and corrected for (solid and open stars) the STAR acceptance in the mass regions of $0.4\text{-}0.76$ (a), $0.76\text{-}1.2$ (b), and $1.2\text{-}2.6$ GeV/c^2 in $60\text{-}80\%$ Au+Au (solid markers) and U+U (open markers) collisions. The systematic uncertainties of the data are shown as gray boxes. The solid and dotted lines are exponential fits to the data in Au+Au and U+U collisions, respectively. The dot dashed and dot-dot dashed lines represent the p_T^2 distributions of photon-photon process from two models within the STAR acceptance in $60\text{-}80\%$ Au+Au collisions. Panel (d): The corresponding slope parameters of p_T^2 distributions within (solid and open circles) and corrected for (lines) the STAR acceptance in Au+Au (solid) and U+U (open) collisions.

⁶³⁰ in the STAR detector over the input e^+e^- pairs with $|y_{ee}| < 1$, as shown in
⁶³¹ the following equation:

$$\varepsilon_{Acc} = \frac{dN/dM_{ee} (p_T^e \geq 0.2 \text{ GeV}/c, |\eta_e| \leq 1, |Y_{ee}| \leq 1)}{dN/dM_{ee} (|Y_{ee}| \leq 1)} \quad (19)$$

⁶³² The acceptance correction factor highly depends on the underlying physics
⁶³³ mechanisms, for instance, the correction factor can vary by a factor of 10 be-
⁶³⁴ tween hadronic two-body decay and two-photon interaction processes. From
⁶³⁵ the physics results in Figs. 58, 59, 60, the observed excess is very likely
⁶³⁶ to be linked to the photon-photon interaction. Under this assumption, the
⁶³⁷ acceptance correction is evaluated via model calculation of photon-photon
⁶³⁸ interaction from Ref. [8]. However, the calculations fall below data points at
⁶³⁹ large p_T^2 values while overshoot data at low p_T^2 , especially at extremely low p_T
⁶⁴⁰ region. The discrepancy could be partially attributed to the fact that only
⁶⁴¹ real photons and lowest-order QED are considered in the Equivalent Photon
⁶⁴² Approximation (EPA) approach. Thus, the pair p_T distributions in the two-
⁶⁴³ photon model calculations are modified to match the measured data for the
⁶⁴⁴ acceptance correction factor evaluations. The systematic uncertainty on the
⁶⁴⁵ acceptance correction is estimated by varying the p_T distribution, resulting in
⁶⁴⁶ $<3\%$ uncertainties for $0 < p_T^2 < 0.0064 \text{ (GeV}/c)^2$ in three mass differentials.
⁶⁴⁷ The acceptance factors as a function as p_T^2 are shown in Fig. 62, while the
⁶⁴⁸ ratios of acceptance correction factors with different p_T distribution inputs
⁶⁴⁹ are shown in Fig. 63.

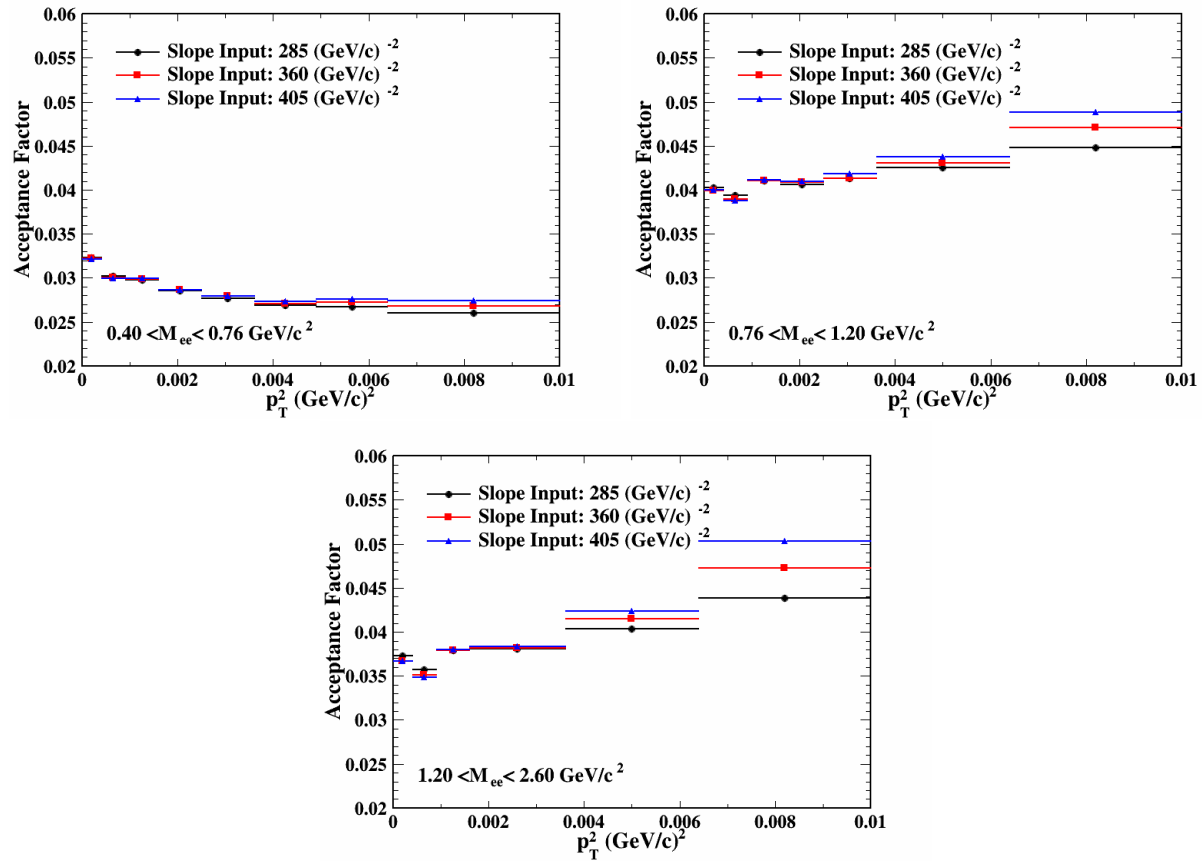


Figure 62: The detector acceptance correction factors derived by the “ $\gamma\gamma \rightarrow e^+e^-$ ” calculations with different pair p_T distributions.

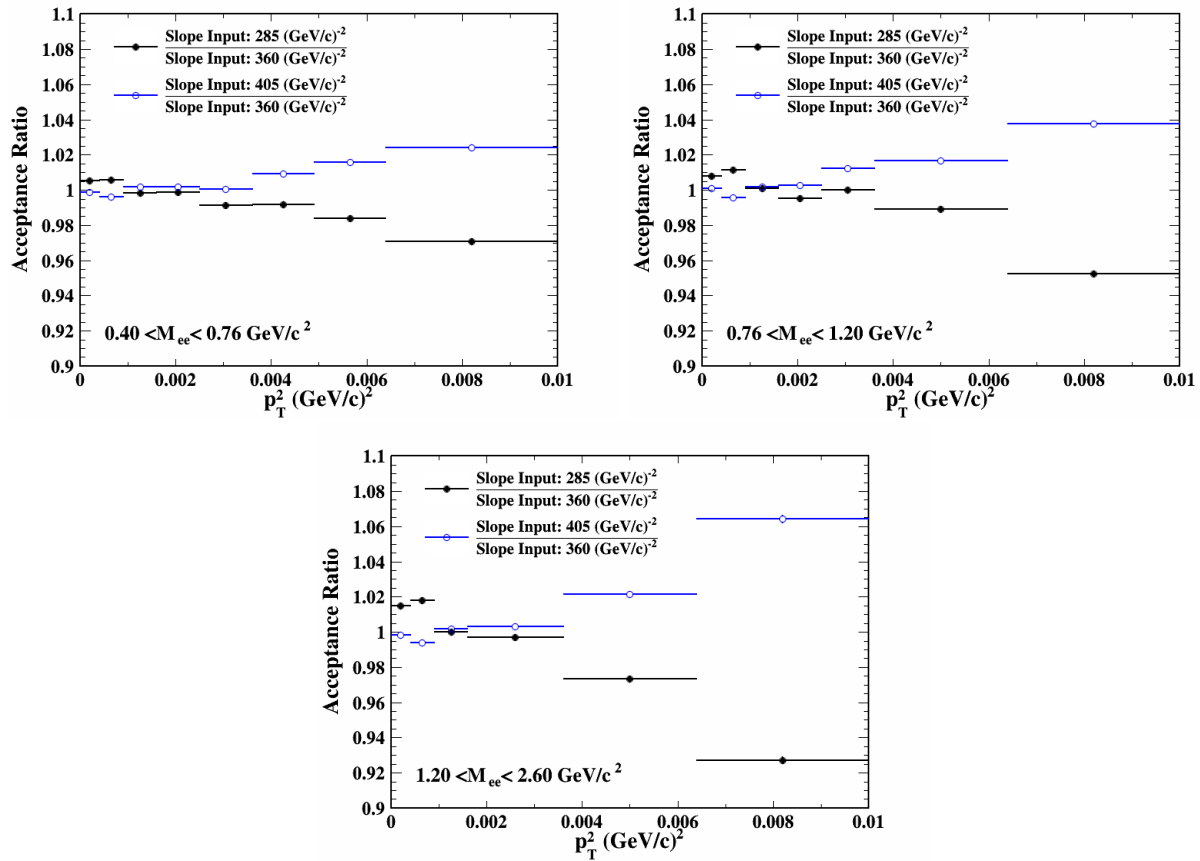


Figure 63: The acceptance correction factor ratios as a function of p_T^2 in three mass differentials.

650 References

- [1] M.L. Miller *et al.*, “Glauber Modeling in High-Energy Nuclear Collisions.” *Annu. Rev. Nucl. Part. Sci.* **57**, 205 (2007).
- [2] L. Adamczyk *et al.* (STAR Collaboration), “Measurements of Dielectron Production in Au+Au Collisions at $\sqrt{s_{NN}} = 200$ GeV from the STAR Experiment.” *Phys. Rev. C* **92**, 24912 (2015).
- [3] A. Adare *et al.* (PHENIX Collaboration), “Detailed measurement of the e^+e^- pair continuum in $p + p$ and Au + Au collisions at $\sqrt{s_{NN}} = 200$ GeV and implications for direct photon production.” *Phys. Rev. C* **81**, 034911 (2010).
- [4] A. M. Poskanzer and S. A. Voloshin, “Methods for analyzing anisotropic flow in relativistic nuclear collisions.” *Phys. Rev. C* **58**, 1671 (1998).
- [5] J. Adams *et al.* (STAR Collaboration), “Azimuthal anisotropy in Au + Au collisions at $\sqrt{s_{NN}} = 200$ GeV.” *Phys. Rev. C* **72**, 014904 (2005).
- [6] CERN Program Library Long Write-up W5013, “GEANT - Detector Simulation and Simulation Tool” http://wwwasdoc.web.cern.ch/wwwasdoc/geant_html3/geantall.html.
- [7] Torbjörn Sjöstrand *et al.*, “High-energy-physics event generation with Pythia 6.1.” *Comput. Phys. Commun.* **135**, 238 (2001).
- [8] W. M. Zha *et al.*, “Coherent lepton pair production in hadronic heavy ion collisions.” *Phys. Lett. B* **781**, 182 (2018).
- [9] S. R. Klein, “Two-photon production of dilepton pairs in peripheral heavy ion collisions.” *arXiv:* 1801.04320.
- [10] D. Kikola *et al.*, “Prospects for quarkonia production studies in U + U collisions.” *Phys. Rev. C* **84**, 054907 (2011).

- [675] [11] Z. B. Tang *et al.*, “Spectra and radial flow in relativistic heavy ion
[676] collisions with Tsallis statistics in a blast-wave description.” *Phys. Rev.*
[677] *C* 79, 051901 (2009).
- [678] [12] Z. B. Tang *et al.*, “The Statistical Origin of Constituent-Quark Scaling
[679] in QGP Hadronization.” *Chin. Phys. Lett.* 30, 031201 (2013).
- [680] [13] B. I. Abelev *et al.* (STAR Collaboration), “Systematic measurements of
[681] identified particle spectra in pp , $d + \text{Au}$, and $\text{Au} + \text{Au}$ collisions at the
[682] STAR detector.” *Phys. Rev. C* 79, 034909 (2009).
- [683] [14] K. A. Olive *et al.* (Particle Data Group), “REVIEW OF PARTICLE
[684] PHYSICS.” *Chin. Phys. C* 38, 090001 (2014).
- [685] [15] N. M. Kroll, W. Wada, “Internal Pair Production Associated with the
[686] Emission of High-Energy Gamma Rays.” *Phys. Rev.* 98, 1355 (1955).
- [687] [16] K Nakamura *et al.*, “Review of Particle Physics.” *J. Phys. G* 37, 075021
[688] (2010).
- [689] [17] R. Arnaldi *et al.* (NA60 Collaboration), “Study of the electromagnetic
[690] transition form-factors in $\eta \rightarrow \mu^+ \mu^- \text{gamma}$ and $\omega \rightarrow \mu^+ \mu^- \pi^0$ decays
[691] with NA60.” *Phys. Lett. B* 677, 260 (2009).
- [692] [18] L.G. Landsberg, “Electromagnetic decays of light mesons.” *Phys. Rept.*
[693] 128, 301 (1985).
- [694] [19] M. N. Achasov *et al.*, “Study of conversion decays $\phi \rightarrow \eta e^+ e^-$ and
[695] $\eta \rightarrow \gamma e^+ e^-$ in the experiment with SND detector at VEPP-2M collider.”
[696] *Phys. Lett. B* 504, 275 (2001).
- [697] [20] L. Adamczyk *et al.* (STAR Collaboration), “Measurements of D^0 and
[698] D^* production in $p + p$ collisions at $\sqrt{s} = 200$ GeV.” *Phys. Rev. D* 86,
[699] 072013 (2012).

- [21] L. Adamczyk *et al.* (STAR Collaboration), “Observation of D^0 Meson Nuclear Modifications in Au + Au Collisions at $\sqrt{s_{NN}} = 200\text{GeV}$.” *Phys. Rev. Lett.* **113**, 142301 (2014).
- [22] S. R. Klein *et al.*, *Comput. Phys. Commun.* **212**, 258 60 (2017).
- [23] F. Krauss, M. Greiner, and G. Soff, *Progress in Particle and Nuclear Physics* **39**, 503 (1997).
- [24] R. C. Barrett and D. F. Jackson, *Nuclear Sizes and Structure* (*Oxford University Press*, 1977).
- [25] S. J. Brodsky, T. Kinoshita, and H. Terazawa, *Phys. Rev. D* **4**, 1532 (1971).
- [26] J. Adams *et al.* (STAR Collaboration), *Phys. Rev. C* **70**, 031902 (2004).
- [27] M. Dyndal *et al.* (ATLAS Collaboration), *Nuclear Physics A* **967**, 281 (2017).
- [28] E. Abbas *et al.* (ALICE Collaboration), *The European Physical Journal C* **73**, 2617 (2013).
- [29] C. Loizides, J. Nagle, and P. Steinberg, *SoftwareX* **1-2**, 13 (2015).